Cryosectioning-enhanced super-resolution microscopy for single-protein imaging across cells and tissues

Johannes Stein[1,2,*], Maria Ericsson[3], Michel Nofal[1], Lorenzo Magni[1], Sarah Aufmkolk[2], Ryan B. McMillan[1], Laura Breimann[2], Conor P. Herlihy[2], S. Dean Lee[2], Andréa Willemin[4,5], Jens Wohlmann[6], Laura Arguedas-Jimenez[4], Peng Yin[1], Ana Pombo[4,5], George M. Church[1,2,*] and Chao-ting Wu[2,*]

[1] Wyss Institute of Biologically Inspired Engineering, Boston, MA, USA.
[2] Department of Genetics, Harvard Medical School, Boston, MA, USA.
[3] Blavatnik Institute, Harvard Medical School, Boston, MA, USA.
[4] Max-Delbrück-Center for Molecular Medicine in the Helmholtz Association (MDC), Berlin Institute for Medical Systems Biology (BIMSB), Epigenetic Regulation and Chromatin Architecture Group, Berlin, Germany.
[5] Humboldt-Universität zu Berlin, Institute for Biology, Berlin, Germany.
[6] Department of Biosciences, University of Oslo, Norway.
*Corresponding authors. Contact: johannes.stein@wyss.harvard.edu (J.S.), gchurch@genetics.med.harvard.edu (G.M.C.), twu@genetics.med.harvard.edu (C.-t.W.)

Abstract

DNA-PAINT enables nanoscale imaging with virtually unlimited multiplexing and molecular counting. Here, we address challenges, such as variable imaging performance and target accessibility, that can limit its broader applicability. Specifically, we enhance its capacity for robust single-protein imaging and molecular counting by optimizing the integration of TIRF microscopy with physical sectioning, in particular, Tokuyasu cryosectioning. Our method, tomographic & kinetically enhanced DNA-PAINT (tkPAINT), achieves 3 nm localization precision across diverse samples, enhanced imager binding, and improved cellular integrity. tkPAINT can facilitate molecular counting with DNA-PAINT inside the nucleus, as demonstrated through its quantification of the in situ abundance of RNA Polymerase II in both HeLa cells as well as mouse tissues. Anticipating that tkPAINT could become a versatile tool for the exploration of biomolecular organization and interactions across cells and tissues, we also demonstrate its capacity to support multiplexing, multimodal targeting of proteins and nucleic acids, and 3D imaging.

Introduction

Spatial omics technologies are advancing our understanding of the molecular principles that govern cellular function and organization[1–3]. By integrating molecular composition with spatial context, these approaches illuminate how biomolecules organize within cells and tissues. Super-resolution microscopy has expanded these capabilities, enabling visualization of biomolecules at sub-20 nm resolution[4–7]. DNA-PAINT (Points Accumulation for Imaging in Nanoscale Topography) is a single-molecule localization microscopy (SMLM) technique that achieves super-resolution imaging via transient binding of dye-labeled "imager" oligonucleotides to complementary "docking strands" attached to the target molecules[8]. DNA-PAINT enables straightforward sequential multiplexing of up to 30 targets[9–11], single-protein resolution[12–14], and molecular counting[15,16], establishing it as a powerful tool for spatial biology.

The potential of DNA-PAINT relies on sample preparations that ensure accessibility to a wide range of targets while retaining cellular ultrastructure. Indeed, challenges such as fixation-induced redistribution of target molecules, antibody-induced clustering, or target loss during permeabilization can affect nanoscale imaging outcomes[17–21]. Additionally, the imaging performance of DNA-PAINT varies

45 across sample types, molecular targets, and microscopy modalities[8,22,23]. For instance, while Total Internal
46 Reflection Fluorescence[24] (TIRF) microscopy offers the highest resolution for single-protein imaging with
47 DNA-PAINT[12,14], its axial range (~200 nm) restricts imaging to targets near the cover glass. Most cellular
48 targets, however, elude the accessible TIRF range and thus require alternative imaging conditions,
49 reducing resolution[8,22,23] and limiting its ability for counting[12,13,25–28].

50   Physical sectioning offers compelling solutions to these challenges[29–32], enabling TIRF-based
51 SMLM imaging of cell regions otherwise inaccessible[33] while ensuring high target accessibility and
52 structural integrity[34,35]. Despite implementations with SMLM across diverse samples[33,36–40], sectioning has
53 thus far only been used for DNA-PAINT imaging of tissues[41–45], where it is a routine step. For instance,
54 Tokuyasu cryosectioning[46] – known for its excellent ultrastructure preservation and antigenicity[35] – was
55 recently adopted for DNA-PAINT, achieving 4 nm localization precisions using TIRF and multiplexing via
56 Exchange-PAINT[9] on ~350 nm rat brain cryosections without permeabilization[47,48]. Additionally, DNA-
57 PAINT imaging of ultrathin resin sections has enabled volumetric reconstructions from sequential sections,
58 as shown in Alzheimer's brain tissues[45]. These studies provide compelling reasons to maximize the
59 potential of physical sectioning for DNA-PAINT.

60   Here, we present "tomographic and kinetically-enhanced DNA-PAINT" (tkPAINT), a workflow that
61 leverages physical sectioning to align sample volume with TIRF illumination, thereby greatly enhancing
62 resolution and imager binding for robust single-protein imaging and counting. Adopting a Tokuyasu
63 protocol for targeting RNA Polymerase II (Pol II) in HeLa cells[49], we demonstrate the potential of physical
64 sectioning for intranuclear DNA-PAINT imaging[22,50–54] (**Fig. 1**a), obtaining localization precisions down to
65 3 nm while preserving cellular ultrastructure. We show that reducing section thickness can enhance
66 imager binding statistics, with up to 80% of localizations attributed to Pol II signal in ~150 nm cryosections.
67 This enabled us to perform molecular counting with DNA-PAINT inside the nucleus. Using qPAINT[15]
68 (quantitative DNA-PAINT), we count antibodies within nanoscopic Pol II clusters and quantify their nuclear
69 abundance. Extending tkPAINT to mouse tissues, we demonstrate its ability to deliver consistent
70 conditions for single-protein imaging and counting across sample types while revealing cell- and tissue-
71 specific heterogeneities in Pol II organization[55,56]. The versatility of tkPAINT is further highlighted through
72 multiplexing, multimodal imaging of proteins and nucleic acids as well as 3D imaging using astigmatism.
73 While this work pushes the capabilities of DNA-PAINT for spatial biology in single sections, we anticipate
74 integrations of tkPAINT with well-established serial sectioning approaches[36,39,45,57] to reconstruct larger
75 sample volumes and entire nuclei.

76

77 **Results**

78 **tkPAINT enables TIRF-based DNA-PAINT throughout ultrastructure-preserved cells with enhanced**
79 **resolution and binding kinetics**

80   To develop tkPAINT, we chose to target the largest subunit of Pol II, Rpb1, a highly abundant
81 nuclear protein. We focused, in particular, on its C-terminal domain (CTD), which features 52 heptad
82 repeats of the consensus motif YSPTSPS, the residues of which are posttranslationally modified during
83 transcription and are involved in promoting co-transcriptional RNA splicing[58] (**Fig. 1**b). Using a primary
84 antibody against hyperphosphorylated Serine-5 of the CTD (S5p), we then leveraged previously optimized
85 protocols for diffraction-limited nuclear imaging within Tokuyasu cryosections under ultrastructure-

86   preserving conditions[59] (**Supplementary Fig. 1**). If not stated otherwise, we refer to ultrathin cryosections
87   of ~150 nm thickness as 'cryosections', which were used for most tkPAINT experiments presented in this
88   work.

89   We labeled whole HeLa cells as well as cryosections of fixed HeLa cells with both primary
90   antibodies and oligo-conjugated secondary antibodies designed for 2D DNA-PAINT imaging using both a
91   classical imager[8] (P1) and speed-optimized imager[60] (R4) which enables faster imaging at reduced imager
92   concentrations and hence reduced fluorescence background (**Methods**). Whole cells were then imaged
93   using DNA-PAINT with HILO illumination, while for tkPAINT, cryosections were imaged using TIRF
94   illumination at a TIRF angle that ensured approximately homogeneous intensity over the section
95   thickness[61]. For HILO imaging we increased imager concentrations by 2-4-fold compared to tkPAINT, due
96   to bleaching of diffusing imagers within the excited HILO volume, reducing the effective imager
97   concentration. At least three datasets were acquired per condition. Duration of data acquisition was kept
98   identical for both HILO DNA-PAINT and tkPAINT imaging and imager concentrations were adjusted
99   individually in each experiment to ensure sparse single-molecule blinking required for obtaining
100   localizations from individual fluorescent molecules[6] (**Methods**).

101   **Figures 1**c and **1**d depict the reconstructed super-resolution images obtained via HILO DNA-PAINT
102   and tkPAINT, respectively. Overall, localizations appeared less clustered and more widely distributed in
103   the HILO DNA-PAINT image presumably due to the larger imaging volume crowded with antibodies and
104   lower resolution. TIRF illumination in tkPAINT led to up to 10× higher signal-to-noise ratio, as compared
105   to HILO (**Supplementary Fig. 2**), translating to an almost 3-fold improvement in localization precision,
106   down to ~3 nm as compared to ~8.3 nm in HILO DNA-PAINT (determined via Nearest Neighbor Analysis[62],
107   NeNA; **Supplementary Fig. 2**). R4 enabled HILO imaging at 10x lower imager concentration compared to
108   P1, increasing the signal-to-noise ratio by more than 4-fold. However, this did not translate to an
109   improvement in localization precision (8.1 nm vs. 8.3 nm, respectively; **Supplementary Fig. 2**), indicating
110   that background fluorescence from diffusing imagers had negligible influence on localization precision
111   compared to other factors such as out-of-focus binding events, autofluorescence or optical aberrations in
112   HILO. To confirm this, we used fluorogenic imager strands[11,63] for HILO imaging, which suppress both
113   fluorescence and photobleaching during diffusion, again achieving localization precisions of ~8 nm
114   (**Supplementary Fig. 3**).

115   As a reference, we performed *in vitro* DNA-PAINT imaging of surface-immobilized DNA origami[64]
116   structures that featured a docking strand pattern with 20 nm spacing[8] using TIRF. This resulted in a
117   localization precision of 2.8 nm (**Extended Data Fig. 1**), demonstrating that tkPAINT can translate the
118   resolution achievable with TIRF under *in vitro* conditions to the nuclei of fixed cells.

119   Efficient nuclear antibody staining in whole cells typically requires strong permeabilization[19],
120   which can disrupt cellular ultrastructure, particularly in the cytoplasm[18] (**Extended Data Fig. 2**). This
121   disruption limits the applicability of multiplexed DNA-PAINT imaging for detergent-sensitive cytoplasmic
122   targets, such as lysosomes[65], alongside nuclear antigens. By enabling intracellular access through
123   sectioning, omitting permeabilization, tkPAINT overcomes this limitation. We demonstrated simultaneous
124   imaging of lysosome-associated membrane protein 1 (LAMP1) and RNA Polymerase II (Pol II) at sub-3 nm
125   localization precision while preserving cellular ultrastructure, as validated by immunogold electron
126   microscopy (**Extended Data Fig. 2**). In the nucleus, permeabilization did not lead to noticeable

127 ultrastructural perturbation and can be used to enhance antigen accessibility throughout cryosections[66]
128 (**Supplementary Figs. 1 & 4**).

129 In addition to enhancing resolution and enabling cell-wide ultrastructural access, ultrathin
130 sectioning inherently improves the kinetic sampling of target molecules. The reduced imaged volume
131 allows higher per-molecule imager-binding frequency while still ensuring isolated single-molecule
132 fluorescence events required for accurate localization (**Extended Data Fig. 3**a). In fact, inspecting
133 individual clouds of localizations in both datasets indicated significantly higher imager binding frequencies
134 as well as number of localizations with tkPAINT as compared to HILO DNA-PAINT (yellow circles and insets,
135 **Fig. 1**c and d, respectively). To confirm this, we globally analyzed both datasets by dividing them into five
136 equal temporal segments and assigning unique colors to each segment (e.g., red for the first segment,
137 blue for the last; total imaging time ~17 min; **Extended Data Fig. 3**b). The highly colored HILO image
138 indicated most target molecules experienced only imager binding events during one of the time segments.
139 In contrast, the tkPAINT image appeared predominantly white, reflecting frequent revisits of imagers to
140 target molecules. The reduction in imaging volume with tkPAINT effectively enhances imager-binding
141 statistics, a crucial factor in DNA-PAINT for both single-molecule profiling at high fidelity and molecular
142 counting, as discussed in the following sections.

143

144
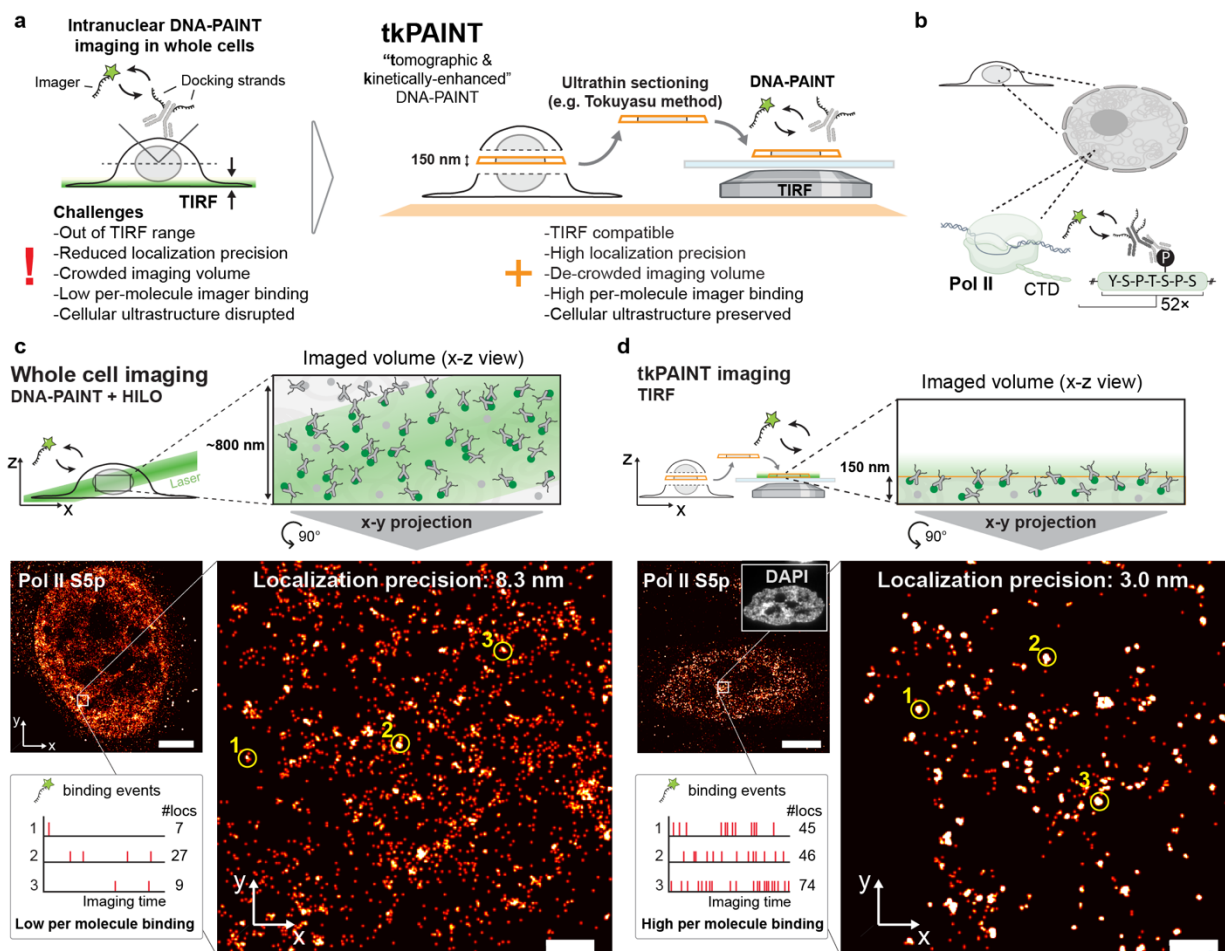
Figure 1 | tkPAINT enables TIRF-based DNA-PAINT imaging of intranuclear targets and enhanced imager binding. a tkPAINT schematic. Ultrathin cryosectioning enables nuclear DNA-PAINT imaging under TIRF conditions. **b** Immunolabeling of Pol II CTD Serine-5 phosphorylation (S5p) for DNA-PAINT imaging via docking strand-conjugated secondary antibodies. **c** HILO DNA-PAINT image of Pol II S5p within whole HeLa cell. Time traces of imager binding and corresponding number of localizations are shown for the three regions indicated by yellow circles, demonstrating low per molecule binding since imager binding events are shared between a high number of labeled target molecules within the imaged volume (green circles, top schematic; grey target molecules inaccessible to antibody labeling remain unseen). **d** tkPAINT image of Pol II S5p. The inset shows the same cell imaged in the DAPI channel. Time traces of imager binding and number of localizations are shown for three regions indicated by yellow circles, demonstrating high per molecule binding. Imager binding events are shared between a low number of imaged target molecules within the imaged volume (green circles, top schematic). Scale bars, 5μm in (**c**,**d**), 400 nm in zoom-ins.

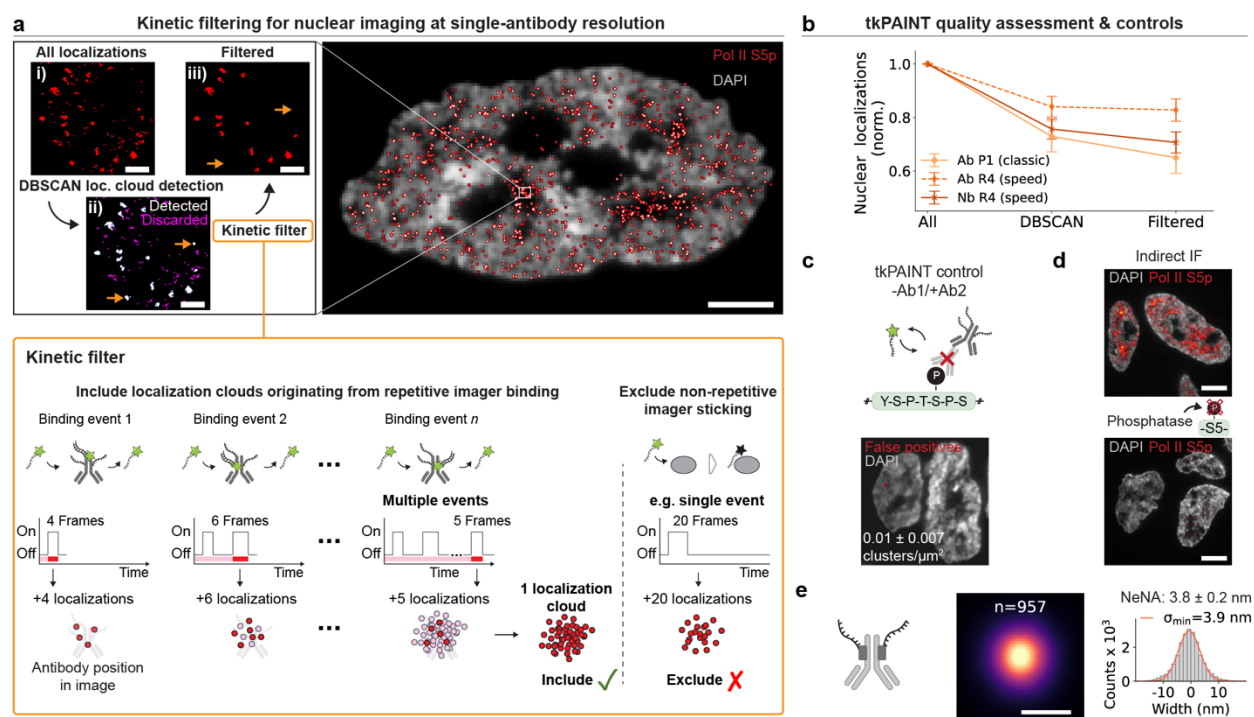**tkPAINT enables nuclear imaging of Pol II at single antibody resolution and molecular counting**

The repetitive binding of imagers in DNA-PAINT is a critical advantage for single-protein imaging, enabling the exclusion of localizations caused by non-repetitive imager sticking[13,67,68]. This is typically accomplished by employing clustering algorithms to identify accumulations of localizations, referred to as 'localization clouds,' which originate from docking strand-conjugated labels. The kinetic fingerprint of each localization cloud is then analyzed to determine whether it exhibits repetitive binding. **Fig. 2a** outlines this two-step analysis approach similar to the one by Fischer *et al.*[13], i) applying the clustering algorithm DBSCAN[69] to detect localization clouds and ii) using a kinetic filter to exclude clouds that lack repetitive binding and are likely attributable to non-specific imager sticking (for detailed analysis steps and parameters see **Supplementary Fig. 5**).

For the tkPAINT datasets imaged with speed-optimized imager R4, over 80 % of nuclear localizations were identified as repetitive localization clouds, demonstrating efficient and targeted imaging (**Fig. 2**b). In comparison, classic imager P1 yielded a post-filtering rate of 60 %, consistent with the expected benefits of speed-optimized imagers[60,70]. Since multiple secondary antibodies can bind to a single primary antibody, this may amplify imager binding at individual target epitopes. To assess this, we repeated tkPAINT imaging using R4-conjugated secondary nanobodies, which limit the number of docking strands to a maximum of two per primary antibody. We indeed observed a minor reduction compared to R4-labeled secondary antibodies, however, still providing an excellent post-filtering localization yield of ~70 %.

However, repeated imager binding on its own is not necessarily indicative of specificity since intrinsic cellular features could potentially also lead to repeated binding. Furthermore, secondary labels could non-specifically bind and thus position docking strands within the sample. To estimate the impact of false positive localization clouds, we performed a set of negative controls under conditions identical to that of previous tkPAINT acquisitions, but on cryosections that were incubated only with secondary antibody/nanobody and no primary antibody (**Fig. 2**c). For all tkPAINT imaging conditions, we found a negligible contribution (~1 %) of false positive localization clouds in both cases as compared to tkPAINT experiments labeled with both primary and secondary antibody/nanobody (**Fig. 2**c and **Supplementary Fig. 6**). Increasing section thickness led to higher localization cloud densities, however, as expected both resolution and kinetic enhancement diminished (**Supplementary Fig. 7**). Thinner cryosections (~80 nm) as used in our immunogold electron microscopy experiments (**Extended Data Fig. 2**) yielded sparse antibody signal and required delicate handling, making 150 nm our default thickness for tkPAINT. Lastly, we tested the specificity of the primary antibody against Pol II S5p by treating cryosections with phosphatase in

5

188 order to neutralize phosphorylation sites prior to staining for indirect immunofluorescence[59].
189 Reassuringly, this led to a 3-fold signal loss (**Fig. 2**d).

190   The sparse distribution of localization clouds after kinetic filtering in tkPAINT (**Fig. 2**a) was
191 reminiscent of immunogold experiments in which antibodies labeled with gold nanoparticles (diameters
192 ~5-15 nm) permit antigens to be detected in cryosections by TEM at the level of single antibodies[35]. To
193 determine whether the resolution possible through tkPAINT would enable single antibodies to be
194 visualized, we performed a range of center-of-mass alignments to obtain averaged sum images for a
195 decreasing minimum number of localizations per cloud (**Supplementary Fig. 8**). We found that
196 localizations in sum images were approximately Gaussian distributed with their standard deviations
197 converging to a minimum. In other words, further reduction of localizations per cloud did not reduce the
198 localization spread. **Figure 2**e displays a convergent sum image with a standard deviation (σ_{min}) of ~3.9 nm
199 and a full width at half maximum of ~9 nm (FWHM ≈ 2.355×σ_{min}), indicating that localizations likely
200 accumulated from individual antibodies, whose physical size is ~10 nm[71]. Since secondary-nanobody
201 labeling reduces the total label size, localization clouds more accurately reflect underlying Pol II S5p
202 epitope positions compared to the increased label size of secondary antibody labeling (**Supplementary
203 Fig. 6**). Together with the controllable number of docking strands per primary antibody (up to two) we
204 thus focused our efforts with tkPAINT to quantify nuclear Pol II S5p based on secondary nanobody labeling
205 (R4).

206

Figure 2 | Nuclear imaging of Pol II at single antibody resolution via tkPAINT. a Schematic of tkPAINT data processing. i) image showing all raw localizations. ii) DBSCAN clustering is applied to detect localization clouds (white) and remaining localizations are discarded (magenta). iii) A kinetic filter[67,68] is applied to discard localization clouds originating from non-repetitive imager sticking (orange arrows in ii) and iii); schematic description in orange box below and detailed in Supplementary Fig. 5). **b** Kinetic filter yield shown for tkPAINT Pol II S5p datasets imaged using different imager sequences (P1 – classic[8] vs. R4 – speed[60]) or different secondary labeling strategies: secondary antibody (Ab) vs. secondary nanobody (Nb). Normalized localization counts with respect to all initial nuclear localizations showing relative loss of localizations in each analysis step. **c** tkPAINT negative control imaging of

215   sample processed with the standard staining protocol but leaving out primary antibody and incubating secondary antibodies only.
216   Mean and standard deviation of number of false positive localization clusters per nuclear area displayed. **d** Top: Diffraction-limited
217   indirect immunofluorescence image of cryosections labeled for Pol II S5p (red) and DAPI (white). Bottom: same as left, but
218   cryosections were treated with phosphatase prior to immunostaining. **e** Resolution benchmarking for Pol II S5p datasets based
219   on secondary nanobody labeling. Middle: rendered sum images of center-of-mass aligned smallest identifiable localization clouds
220   (see Supplementary Fig. 8 for details and additional datasets. Number of localization clouds in sum image stated above). Right:
221   histogram showing the corresponding distribution of localizations fitted with a Gaussian (red curve) to obtain its standard
222   deviation σ_{min}. Scale bars, 5 μm in (**a,e**), 3 μm in (**d**) and 10 nm in sum image in (**e**).

223

224   Since several antibodies can likely bind to a single CTD or to several Pol II molecules close by, we
225   asked whether we could exploit the enhanced imager binding kinetics in tkPAINT to count the number of
226   Pol II antibodies in larger localization clouds (**Fig. 3**a). In qPAINT[15] (quantitative DNA-PAINT), the average
227   imager binding frequency for the smallest identifiable localization clouds in a dataset is taken as a
228   reference (**Fig. 3**b). Assuming the reference represents single antibodies, a localization cloud with N
229   antibodies would have an N-times higher binding frequency[15].

230   We first turned to DNA origami featuring up to 12 DSs to validate the applicability of qPAINT
231   analysis under our experimental tkPAINT conditions. Furthermore, on DNA origami single DSs can be
232   unambiguously chosen as reference clouds. **Fig. 3**b displays the counting results obtained via qPAINT
233   analysis, confirming the expected number of on average ~8 DSs per origami which was in good agreement
234   with visual inspection (see **Supplementary Fig. 9** for additional 400 randomly selected origami and
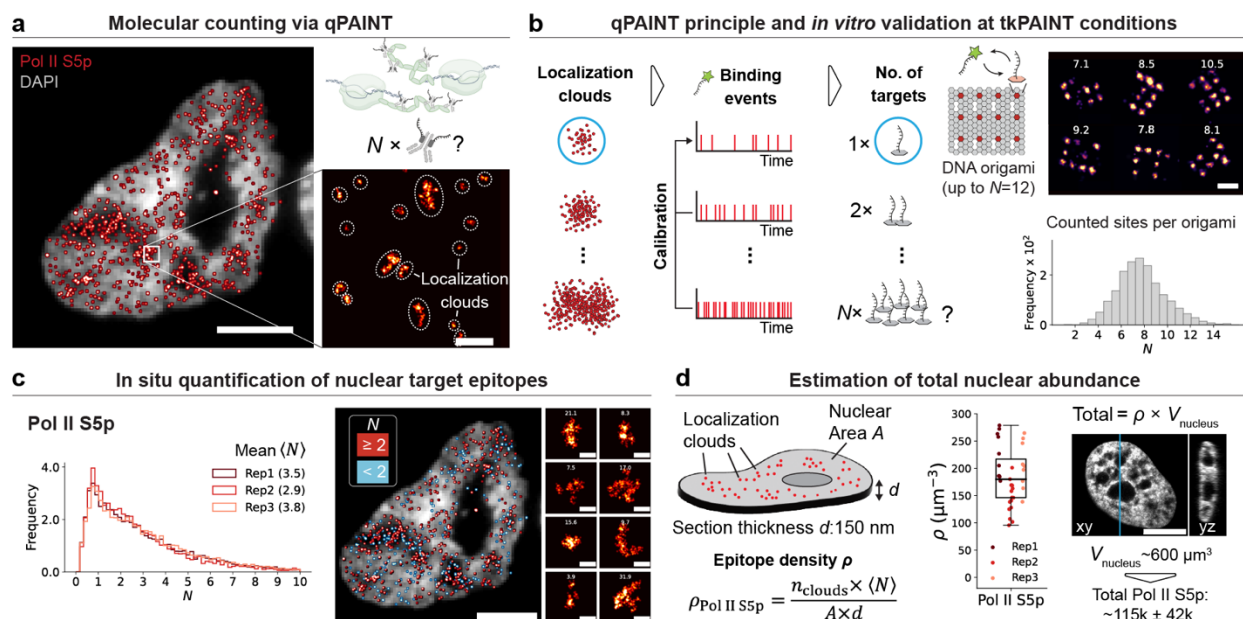235   analysis schematic), confirming our ability to perform molecular counting.

236   In tkPAINT Pol II S5p datasets most sparse localization clouds likely corresponded to single
237   antibodies according to the previously observed spatial localization spread. We thus performed qPAINT
238   analysis using Pol II S5p localization clouds with a convex hull area smaller than the 20th percentile as the
239   qPAINT reference (see **Supplementary Fig. 10** for a detailed analysis schematic). Comparing the imager
240   binding frequency of single docking strands on DNA origami with the one measured for single antibodies
241   in tkPAINT datasets we obtained on average ~1.6 bound nanobodies per primary antibody
242   (**Supplementary Fig. 10**).

243   **Figure 3**c displays the counting results (N) obtained from three independent experiments, each
244   with a prominent single antibody peak and a decreasing tail of localization clouds containing higher
245   numbers of antibodies. The N distributions were in close agreement, with on average 3.2 ± 0.4 antibodies
246   per localization cloud. Localization clouds containing tens of antibodies indicated hot spots of active Pol II
247   (Fig. 3c). Based on these counting results and the known cryosection dimensions, we measured an average
248   nuclear antibody density of 165 ± 45 μm^{-3} (**Fig. 3**d). This translated to ~115,000 ± 42,000 Pol II S5p
249   antibodies per nucleus, which aligns with earlier estimates of ~65,000 engaged Pol II[72] and ~320,000
250   copies of Rpb1[73] per HeLa cell.

251   It is likely that our quantification underestimated the true abundance of phosphorylated S5 (in
252   theory up to 52x per CTD) due to steric effects. Smaller primary labels such as nanobodies against S5p
253   could further improve quantifications and reduce linkage errors. Notably, we could not determine
254   whether the CTD of one or multiple Pol II molecules is present in a localization cloud; however, future
255   studies using C-terminally tagged Pol II cell lines[74] could allow to address this question.

256   Finally, our data enabled us to assess the spatial distribution of Pol II S5p, which is known to
257   associate with active chromatin or nuclear compartments, such as transcription factories and nuclear
258   speckles[58]. Such nuclear regions correlate with low intensities when stained for DNA using DAPI (4',6-

diamidino-2-phenylindole). Indeed, we observed both higher antibody counts (**Fig. 3**c) and a higher overall localization cloud density as determined by nearest neighbor distance analysis[75] for these regions (**Extended Data Fig. 4**).


Figure 3 | Counting Pol II antibodies in nanoscopic complexes and total nuclear abundance. a tkPAINT Pol II S5p datasets contain heterogeneous localization clouds and qPAINT can be exploited to count antibodies localization cloud. **b** Validating the qPAINT using DNA origami imaged under tkPAINT conditions. Left: qPAINT principle[15]. The smallest identifiable localization clouds, i.e. single docking strands on DNA origami (blue circle), serve as a calibration to measure the average imager binding frequency. Relative counting can be performed by comparing the binding frequency of each individual localization cloud to the calibration binding frequency. Right: Distribution of docking strand counts per DNA origami obtained via qPAINT analysis. Right: including six exemplary origami with their respective counting result stated above. **c** Left: Distribution of antibody counts per localization cloud for three Pol II S5p tkPAINT datasets obtained via qPAINT analysis. Right: image displayed in (a), re-rendered by coloring localization clouds according to their antibody counts: red (≥2), blue (<2). The small images on the right shows six exceptionally large localization clouds with antibody counts stated above. **d** Physical sectioning enables straightforward quantification of total nuclear target abundance by calculating the antibody density for the target epitope $\rho_{Pol\ II\ S5p}$ by knowing the number localization clouds, the average number of antibodies per localization cloud. the nuclear area and the section thickness. $\rho_{Pol\ II\ S5p}$ for the three datasets in (c) is shown. Measuring the average nuclear volume of intact HeLa cells via confocal microscopy enables estimation of total nuclear abundance (x-y and x-z representation shown along the slice indicated by the blue line. The volume was averaged over 15 nuclei). Scale bars, 3 μm in (**a,c,d**), 100 nm in zoom-in in (**a**) and 40 nm in zoom-ins in (**b,d**).

Resolution and kinetic enhancement translate to tkPAINT imaging in mouse tissues

Encouraged by successful applications of DNA-PAINT to semi-thin (~350 nm) Tokuyasu tissue sections[47,48], we hypothesized that tkPAINT could also enable kinetic filtering, single-antibody resolution and molecular counting in tissue samples. To test this, we prepared two mouse tissue types (cerebellum and spleen) following established protocols[76] (**Methods**) and processed 150 nm cryosections for tkPAINT tissue imaging of Pol II S5p, using R4-secondary nanobodies. **Figure 4**a depicts super-resolved tkPAINT images of Pol II S5p within cerebellum and spleen cryosections (two datasets were acquired per tissue type). As expected[47], we obtained similar localization precisions as previously in HeLa sections (~3 nm). The kinetic enhancement enabled by physical sectioning also translated to tissue imaging: ~55 % of

8

289 nuclear localizations could be assigned to repetitive localization clouds, confirming the suitability of tissue
290 data for quantitative analysis (**Fig. 4**b). The lower kinetic filtering yield compared to HeLa (~70 %) indicated
291 slightly elevated sticking of R4 in both tissue types. We also performed center-of-mass alignments to
292 obtain averaged sum images with decreasing minimum number of localizations per cloud to find the
293 converging distribution width (**Supplementary Fig. 11**), further confirming tkPAINT's capability for single-
294 antibody resolution in tissues ($\sigma_{min} \approx 3.4$ nm and FWHM≈ 8 nm; **Fig. 4**c).

295 Finally, we performed qPAINT analysis to obtain spatially-resolved antibody counts in the nuclei
296 of both tissue types (**Fig. 4**d). Each tissue yielded reproducible qPAINT distributions and averaged ~4.2
297 antibodies per localization cloud, higher than the ~3.2 observed in HeLa cells for the Pol II S5p epitope
298 (**Fig. 3**c). Interestingly, while the qPAINT distribution for spleen closely matched that of HeLa cells, with a
299 single antibody peak and a long tail of higher antibody counts, the cerebellum datasets showed a second
300 peak at ~2.5 antibodies (arrows, **Fig. 4**d). We observed a nearly two-fold enriched average nuclear density
301 in cerebellum nuclei (95 ± 53 μm^{-3} and 173 ± 45 μm^{-3}) and a higher cell-to-cell variability in spleen cells.
302 These findings might reflect an intrinsic heterogeneity of transcriptional activity between tissue types
303 and/or a higher number of cell types within the spleen (**Fig. 4**d). Furthermore, our results demonstrate
304 that tkPAINT provides consistent imaging performance across diverse sample types and paves the way for
305 probing molecular organizations between cultured cells and tissues.

306
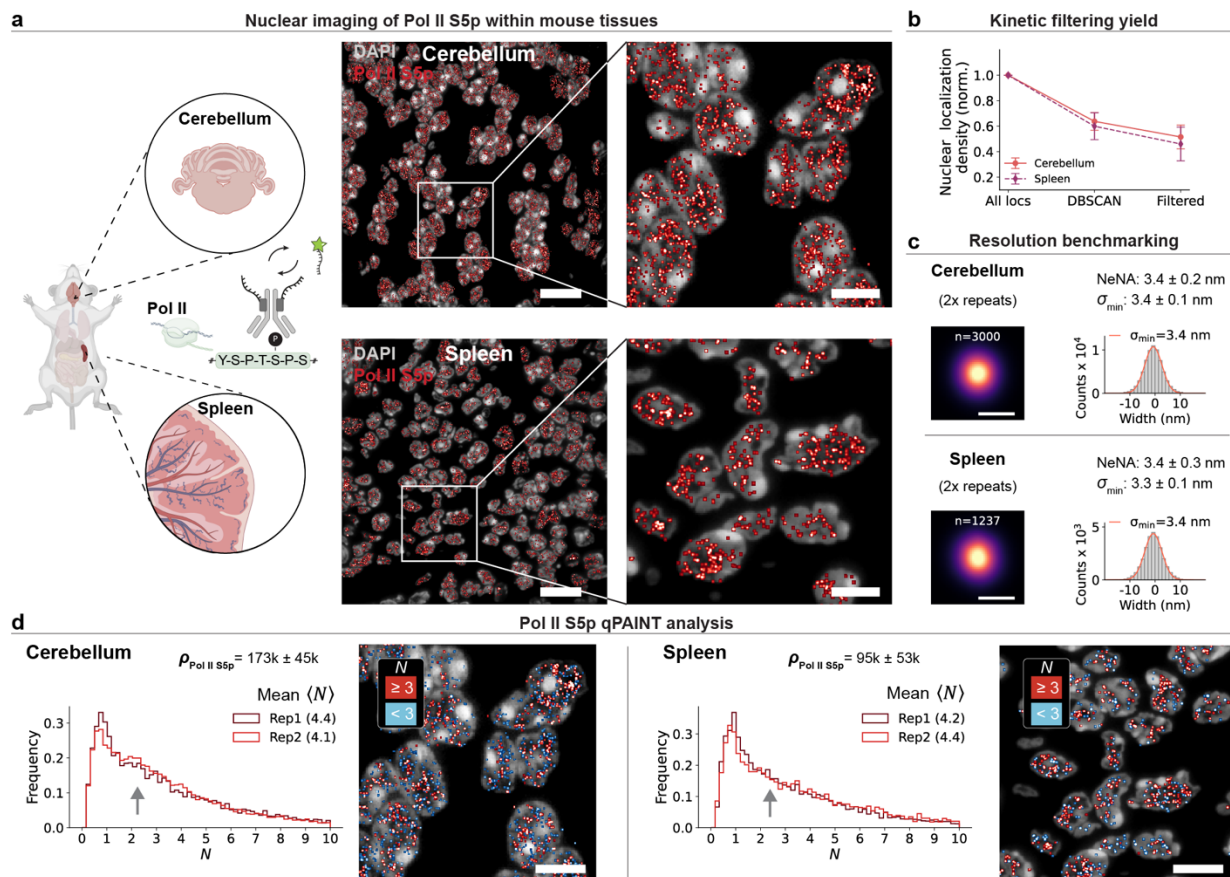
307
308 **Figure 4 | Single-protein resolution and kinetic enhancement translate to tkPAINT tissue imaging. a** Tissue blocks of mouse
309 cerebellum and spleen were processed for Tokuyasu sectioning and subsequently stained for Pol II S5p prior to imaging. Top:

310 tkPAINT image of region of mouse cerebellum and zoom-in to white box. Bottom: tkPAINT image of a region of mouse spleen and
311 zoom-in to white box. **b** Kinetic filtering yield for cerebellum and spleen tkPAINT datasets (2x each). Normalized localization
312 counts with respect to all nuclear localizations showing relative localizations loss in each analysis step. **c** Resolution benchmarking
313 for cerebellum and spleen tkPAINT datasets (top and bottom, respectively). Left: rendered sum images of center-of-mass aligned
314 localization clouds for one data set each. Right: histograms showing the corresponding distribution of localizations fitted with a
315 Gaussian (red curve) to obtain its standard deviation σ_{min} (see Supplementary Fig. 7 for details and Supplementary Fig. 10 for all
316 datasets). **d** qPAINT distributions showing number of Pol II S5p antibodies per localization cloud for cerebellum and spleen
317 datasets. The antibody density $\rho_{Pol\,II\,S5p}$ is stated above. Scale bars, 10 µm in (**a**), 5 µm in zoom-ins in (**a**) and 10 nm in (**c**).

Multiplexed and multimodal tkPAINT for nuclear nanoscale imaging in 2D and 3D.

320 Next, we turned our attention toward several proof-of-concept demonstrations, showcasing the
321 versatility of nuclear tkPAINT imaging with respect to multiplexed single-protein imaging. Circumventing
322 use of any secondary label for Exchange-PAINT[47,77], we conjugated primary antibodies targeting the
323 nuclear lamina (Lamin A/C) and nuclear speckles (SC35[78]), each with an orthogonal docking strand
324 sequence in order to enable multiplexed imaging by sequential exchange of the complementary imager
325 strands for each imaging round (**Fig. 5**a). Exchange-PAINT has the advantage of being free of chromatic
326 aberrations since all imaging rounds can be acquired in the same color channel[9]. **Figure 5**b shows a
327 multiplexed Exchange-tkPAINT image of Lamin A/C, Pol II S5p and SC35, sequentially imaged and
328 subsequently reconstructed using pseudo colors. Not only did sequential imaging enable us to perform
329 quantitative analysis for all three nuclear antigens in parallel, it permitted the spatial probing of
330 intermolecular relationships and features. **Extended Data Fig. 5** provides an overview on how multiplexed
331 tkPAINT data can aid the study of nuclear organization. For example, we observed two peaks in the
332 distribution of nearest neighbor distances for Lamin A/C, which allowed us to separate the signal into a
333 nucleoplasmic and lamina-association fraction[79,80]. Measuring nearest neighbor distances between Pol II
334 S5p and SC35 indicated a spatial organization of Pol II S5p around nuclear speckles with SC35 at their
335 center, as previously observed with TSA-Seq[81].

336 Beyond multiplexed protein imaging, a potentially even more powerful aspect of cryosections is
337 that the same sections can be subject to both immunostaining and fluorescence in situ hybridization[82,83],
338 enabling analyses of the interplay between targeted proteins and specific sequences of RNA and/or DNA.
339 Here, we performed proof-of-principle tkPAINT imaging of α-tubulin in cryosections that had additionally
340 been labeled for telomeric repeats via in situ hybridization (**Fig. 5**c). Similarly, hybridization of a poly(dT)
341 probes enabled us to perform tkPAINT imaging of mature mRNA (**Fig. 5**d).

342 TkPAINT data, previously generated through 2D imaging and, thus, resembling a two-dimensional
343 projection of molecules within cryosections, could be significantly enhanced by accessing the axial
344 dimension for a true interrogation of nanoscale organization. To this end, we constructed a simple and
345 affordable (~700$) custom addition to our commercial TIRF system that allowed us to insert a cylindrical
346 lens in front of the camera for astigmatic 3D imaging[84] (**Supplementary Fig. 12**). We first benchmarked
347 our 3D imaging capability, again using surface-immobilized DNA origami with 20-nm docking strand
348 spacing. Although the docking strand arrangement, itself, was in 2D, it nevertheless allowed us to
349 determine the achievable axial resolution in z as well as assess whether astigmatism would significantly
350 reduce our lateral resolution. **Figure 5**e shows an averaged 3D DNA-PAINT sum image of (~450 origami),
351 demonstrating that individual docking strands could be laterally visualized at $FWHM_{x,y} \approx 8.5$ nm
352 ($\sigma_{x,y} \approx 3.6$ nm), which was sufficient to resolve the 20-nm-spaced pattern (**Fig. 5**f). During DNA origami
353 experiments, we observed that glass slides could be tilted with respect to the optical axis, as revealed

354 when we colored localizations according to their axial position (**Fig. 5**f). To account for this tilt, we
355 performed a z-correction by fitting and subtracting a 2D plane[85] (**Fig. 5**f and **Supplementary Fig. 13**). Post
356 tilt-correction, 3D DNA-PAINT imaging of DNA origami yielded an axial distribution of localizations at
357 $FWHM_z \approx 20$ nm ($\sigma_z \approx 8.5$ nm), in line with the known ~2× axial resolution drop for astigmatic 3D SMLM[84].
358 An axial resolution of 20 nm would nevertheless allow us to determine distinct axial positions of
359 antibodies within cryosections with a thickness of ~150 nm.

360 These validations enabled us to move on to 3D tkPAINT imaging within cryosections of fixed HeLa
361 cells, repeating sequential imaging of Lamin A/C, Pol II S5p, and SC35 (**Fig. 5**g). The left image in **Figure 5**g
362 shows the super-resolved Pol II S5p image rendered with a range of colors according to the z-position of
363 each localization over an axial range of 150 nm. It has been shown that, for unpermeabilized cryosections,
364 antibody labeling happens predominantly at both surfaces of sections[86]. However, the permeabilization
365 step in our protocol ensured antibody penetration throughout the sections, as seen for both localization
366 clouds of all colors in the Pol II S5p image alone and the x-z projection of the multicolor Exchange-tkPAINT
367 image (**Fig. 5**g, left and right, respectively; see **also Supplementary Fig. 4**). Overall, our 3D tkPAINT results
368 are in close agreement with the cryotome setting for a cutting thickness of 150 nm. Measuring the overall
369 z-distributions, we observed that while Lamin A/C and Pol II S5p labeling penetrated more
370 homogeneously, SC35 exhibited stronger staining toward the top half of the section (**Supplementary Fig.
371 14**). This result reinforces the additional benefit of using smaller labels such as primary nanobodies in the
372 future.

373

374
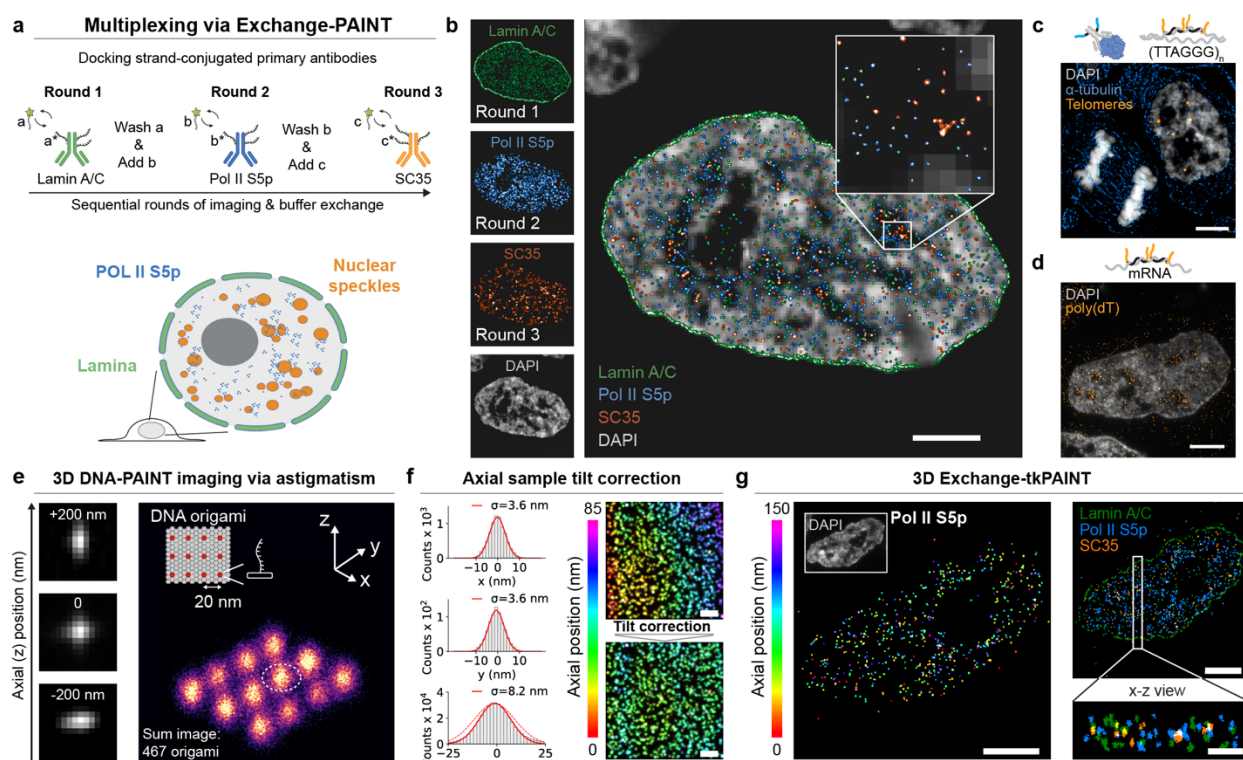
Figure 5 | Multiplexed and multimodal nuclear nanoscale imaging in 2D and 3D. a Schematic of Exchange-tkPAINT targeting
376 Lamin A/C, Pol II S5p and SC35. Primary antibodies are conjugated with orthogonal docking strands (sequences *a**, *b** and *c**)
377 and sequentially imaged with imager strands *a*, *b* and *c*. Previous imager is washed out and subsequent imager is added between

11

378 rounds of imaging. **b** Multiplexed tkPAINT image reconstructed from three rounds of sequential imaging. **c** Combined imaging of
379 protein and DNA using tkPAINT targeting of α-tubulin and telomere repeats via FISH. **d** tkPAINT imaging of mRNA via poly(dT)
380 hybridization probes. **e** Validation of cylindrical lens addition to a commercial TIRF system for 3D DNA-PAINT imaging. Left:
381 Astigmatism-based encoding of axial position by reshaping the point spread function. Right: Sum DNA-PAINT 467 DNA origami
382 with 20 nm docking strand pattern. **f** Left, top and middle: x and y line plot histograms across docking strand position indicated
383 by white dashed circle in (a). Left, bottom: Axial distribution of z coordinates of DNA origami data set. The standard deviation
384 obtained by a Gaussian fit (red curve) is given above the histograms. Right: correction of axial sample tilt affecting measured z-
385 distributions (red dashed curve in c). **g** Left: 3D tkPAINT of Pol II S5p. The color code indicates axial position of antibody signal
386 over a range of 150 nm. Right: 3D Exchange-tkPAINT image of Lamin A/C (green), Pol II S5p (blue) and SC35 (orange). Side view
387 (x-z) of localization clusters projected from white box. Scale bars, 5 μm in (**b**), 3 μm in (**c**) and 150 nm in zoom-in.
388

Discussion

390   With tkPAINT, we used ultrathin sectioning to align sample volume with TIRF illumination,
391 maximizing the capability of DNA-PAINT for single-protein imaging and counting across diverse samples
392 and molecular targets. By leveraging the Tokuyasu method[46], we overcame the range constraint of TIRF
393 to access distal intracellular regions[33], such as the nucleus, and demonstrated tkPAINT imaging throughout
394 ultrastructure-preserved HeLa cells down to 3 nm localization precision. For imaging nuclear antigens such
395 as Pol II, this enabled up to three-fold improved resolution as compared to HILO imaging in whole cells.
396 Physical sectioning not only enhanced resolution and antigen accessibility but also de-crowded the sample
397 volume, improving imager binding statistics critical for robust single-protein imaging[13,14] and counting[15,68].
398 This allowed us to count antibodies within nanoscopic Pol II clusters as well as to quantify cell- and tissue-
399 specific heterogeneities in Pol II organization. Additionally, sequential multiplexing[9] facilitated combined
400 imaging of proteins and nucleic acids, while astigmatism-based axial encoding[84] enabled imaging in 3D.

401   TkPAINT holds significant potential for advancing multiplexing strategies for spatial proteomics
402 with DNA-PAINT. Current sequential DNA-PAINT schemes have, achieved up to 30-plex imaging[10,11]. Single
403 antibody resolution in tkPAINT could enable incorporation of barcoding[87–89] or in situ sequencing[90–92]
404 approaches, potentially scaling to hundreds of targets in fewer rounds. Computational methods[93,94] and
405 isotropic 3D imaging[95–98] could further refine axial encoding. Additionally, tkPAINT could be combined with
406 RESI[14] to reach Ångstrom resolution or complement nanoscopy approaches such as MINFLUX[99],
407 particularly for densely-packed targets. Finally, parallel sample preparation could offer unique
408 opportunities for correlative super-resolution and electron microscopy[34,40,100,101], further broadening
409 tkPAINT's versatility.

410   Limitations of our study include the steric hindrance and variability in specificity inherent to
411 antibody labeling. Smaller, stoichiometric labels, such as nanobodies[102], genetic tags[103], or unnatural
412 amino acids[104], could address these challenges, improving both structural resolution and molecular
413 counting. High-pressure freezing and freeze substitution[105,106] offer a promising route to further minimize
414 fixation artifacts and capture molecular organization closer to the *in vivo* state[20,49]. The reduced imaging
415 volume of tkPAINT compared to whole-cell imaging limits visualization of low-abundance targets and
416 larger structures such as entire genomic regions[54]. Furthermore, compartments such as larger nuclear
417 speckles might appear as multiple smaller structures in a single section. Serial cryosectioning[32,40,107] could
418 address this but would require optimization in order to mitigate challenges such as partial sample loss and
419 folding during manual handling. Combining ultramicrotomy with resin embedding as in array
420 tomography[45,57] may provide an alternative, though at reduced antigenicity[35]. Implementation of machine
421 learning[48,108,109] and automated imager exchange[44] could accelerate tkPAINT imaging to promote

volumetric reconstructions. Nevertheless, the wealth of information gained from super-resolution studies that are based on imaging single nuclear 'optical sections' highlight the strong potential for studying molecular principles of genome organization in single sections alone[51–53,110–115].

Our work enhances the potential of DNA-PAINT for single-protein imaging in various aspects. Through sectioning, we decoupled imaging performance from target selection, achieving optimal conditions for probing nanoscale organization even in dense intracellular environments. Unlike whole-cell nuclear immunolabeling, which requires disruptive permeabilization[19], tkPAINT leverages permeabilization-free access to the nucleus in ultrastructure-preserved cells. This unique feature could enable functional studies linking nuclear and cytoplasmic mechanisms. The integration of in situ hybridization with immunolabeling extends this potential for multimodal investigations of protein–nucleic acid interactions. Finally, consistent imaging performance in both cultured cells and tissues demonstrates tkPAINT's potential for comparative studies between cultured cells and tissues. In conclusion, we believe tkPAINT's broad applicability will help drive DNA-PAINT toward becoming a routine tool for biological discovery.
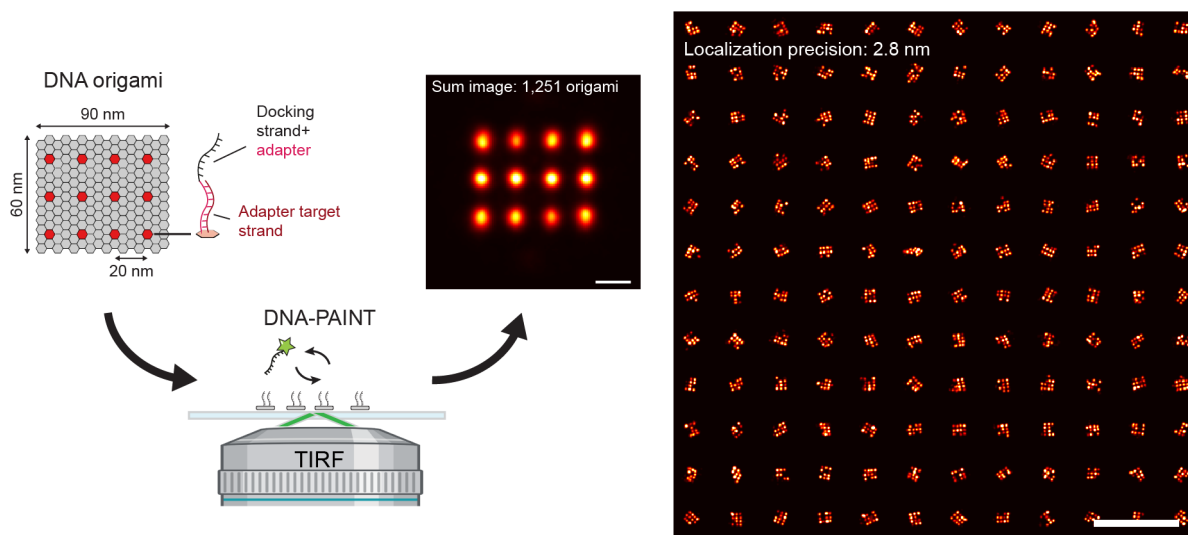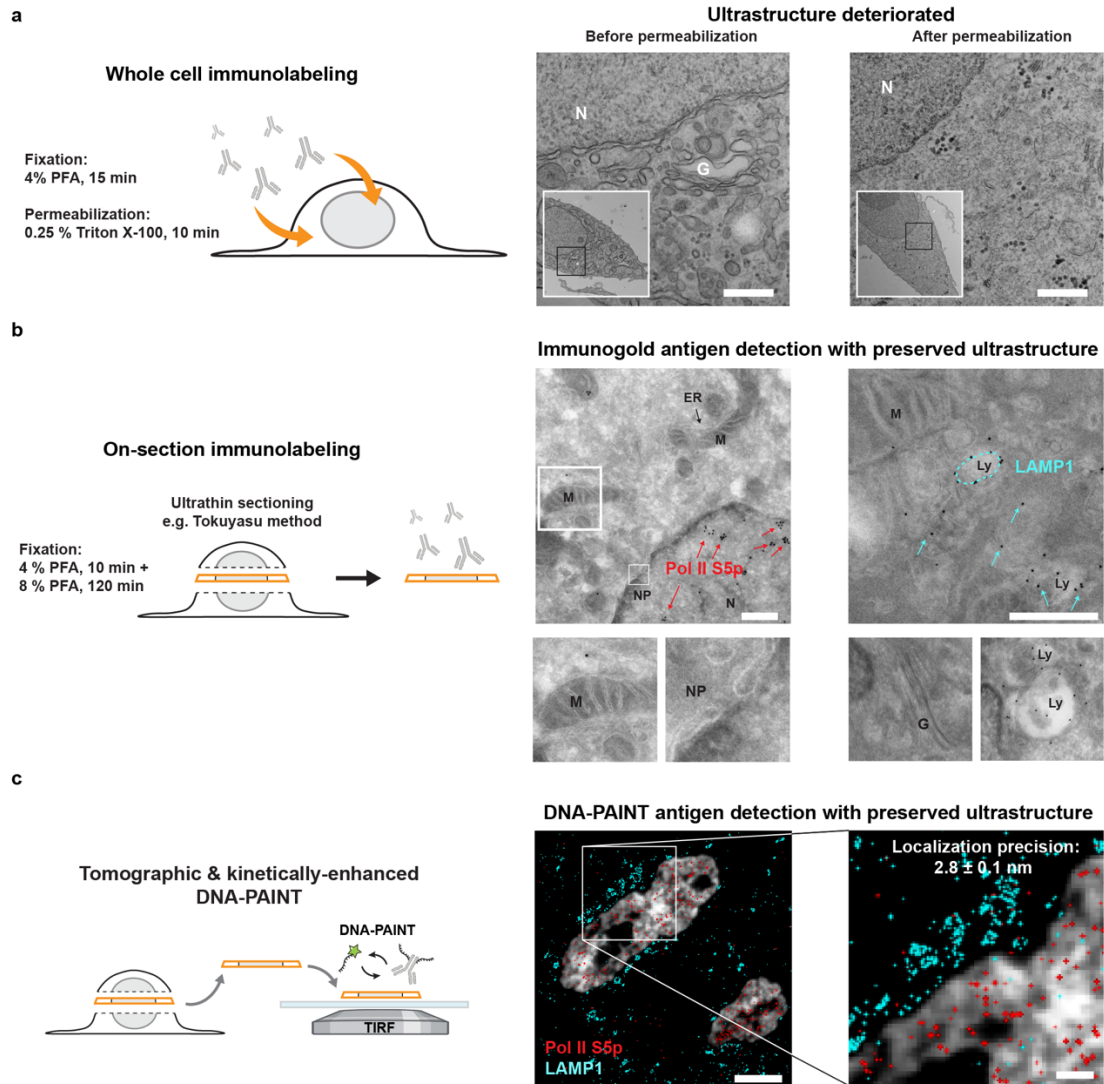
Extended data

Extended Data Fig. 1 | TIRF-based DNA-PAINT imaging of synthetic DNA origami 20 nm grids. DNA-PAINT image of surface-immobilized DNA origami featuring a pattern of docking strands at 20-nm spacing ('20 nm grids'[8]) acquired on our TIRF system. The origami is designed in a modular fashion by carrying 12 anchored 20nt adapter target strands (dark red) to which docking strand-adapter hybrid oligos can be stably hybridized. This way the same origami structure can be used to test different imager-docking strand combinations (see **Methods**). The increased distance between docking strand and anchor point on the origami does not lead to a noticeable decrease in resolution since the hybridized docking strand is still able to rapidly rotate around the anchor point such that on average emitted photons still allow to precisely pinpoint the anchor point[116]. Note that for space reasons some origami illustrations within this work do not show the adapter explicitly, but this origami design was exclusively used for all DNA origami experiments shown. The left image displays an averaged sum image of 1,251 origami and the right image a random selection of 144 origami arranged in 12x12 square. The localization precision for the data set is stated in the right image. Scale bars, 20 nm in left image and 200 nm in right image.

Extended Data Fig. 2 | tkPAINT enables cell-wide DNA-PAINT imaging under ultrastructure-preserved conditions at sub-3 nm localization precision. a Ultrastructural disruption in standard paraformaldehyde(PFA)-based immunofluorescence protocols for whole cells[18]. Transmission electron microscopy (TEM) images of HeLa cells depict how brief fixation times lead to poor structural integrity and permeabilization with Triton X-100 causes reductions in cytoplasmic density as well as apparent organelle loss. Nuclear ultrastructure is relatively well-preserved even for brief fixation and permeabilization (Supplementary Fig. 4). **b** Physical sectioning enables "on-section" labeling of intracellular antigens without permeabilization. TEM images show Tokuyasu cryosections of HeLa cells prepared following a PFA-based fixation protocol optimized for ultrastructural preservation. Immunogold reveals sites of cytoplasmic LAMP1 and nuclear Pol II S5p; Mitochondria (M), nuclear pores (NP), Endoplasmic Reticulum (ER). Golgi and lysosomes (Ly) are highlighted. **c** tkPAINT principle: physical sectioning (e.g. using the Tokuyasu method) enables TIRF-based DNA-PAINT imaging of ultrastructurally-preserved specimens, even without permeabilization. The localization precision of 2.8 ± 0.1 nm was measured over four independent repeats (mean and std., respectively). Scale bars, 200 nm in (a), 400 nm in (b), 2 μm in (c) and 100 nm in zoom-in.

14
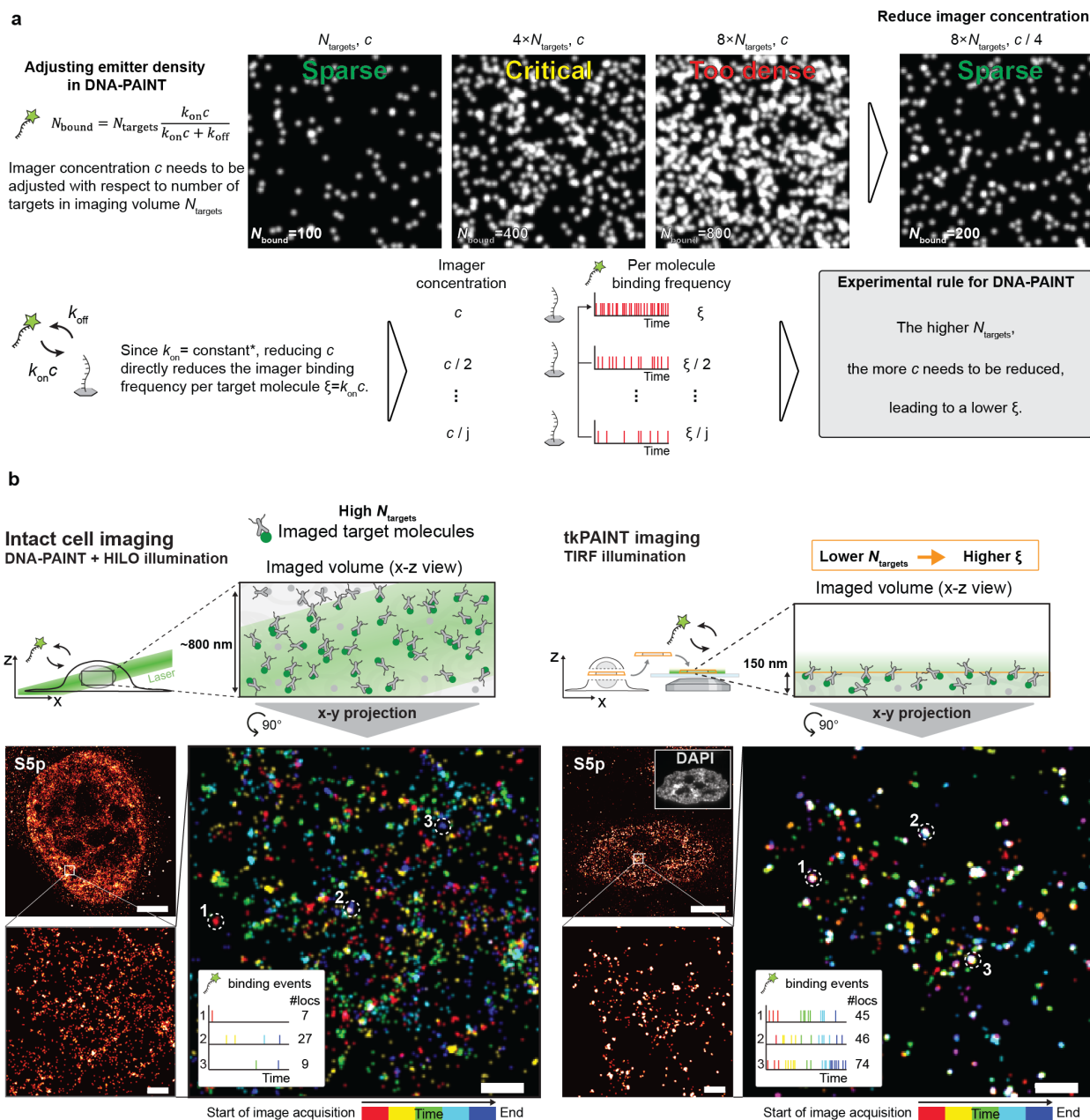
**Extended Data Fig. 3 | Volume reduction in tkPAINT enhances per-molecule imager binding frequencies. a** Simulated raw DNA-PAINT images showcasing that the number of bound imagers at any given time, N_{bound}, must be low enough to ensure sparse single-molecule blinking required for SMLM reconstruction. $N_{bound} = N_{targets} \frac{k_{on}c}{k_{on}c+k_{off}}$, where $N_{targets}$ is the number of labeled target molecules within the imaging volume, k_{on} is the imager association rate, c the imager concentration and k_{off} is the imager dissociation rate. *Note that k_{on} and k_{off} of a given imager-docking strand pair are constant for set experimental conditions such as temperature and buffer conditions[68]. For samples featuring a dense abundance of target molecules, N_{bound} can become too large and blinking events too dense, such that c needs to be reduced. However, a reduction in c inevitably leads to a decrease in the per-molecule imager binding frequency $\xi = k_{on}c$. The number of randomly distributed emitters is stated in the bottom left corner of each simulated image and the image dimension are 16.64 μm x 16.64 μm. **b** Same HILO DNA-PAINT image and tkPAINT image as shown in **Fig. 1**c and d, respectively. Localizations in the zoom-in were color-coded according to registration time during data acquisition (five colors, e.g. red for first and blue for last temporal segment; total imaging time: ~17 min. The HILO DNA-PAINT image displays largely discretely colored localizations, which is expected since the large axial imaging volume in HILO bears a large $N_{targets}$, requiring to image at low imager binding frequency ξ that is not sufficient to repeatedly sample targeted molecules with imager binding events within the time of image acquisition. The tkPAINT image, in contrast, features concentrated

15

485 accumulations of localizations of which many are revealed by temporal coloring as repetitive 'white-colored' localization clusters.
486 The volume reduction in tkPAINT can thus be an effective way of enhancing imager binding statistics by reducing $N_{targets}$ and
487 thus allowing to image at higher per-molecule imager binding frequencies. For both images, time traces of imager binding and
488 number of localizations are shown for three regions indicated by white circles, indicating high per molecule binding. Scale bars,
489 5 μm in (**b**) and 400 nm in zoom-ins.

490
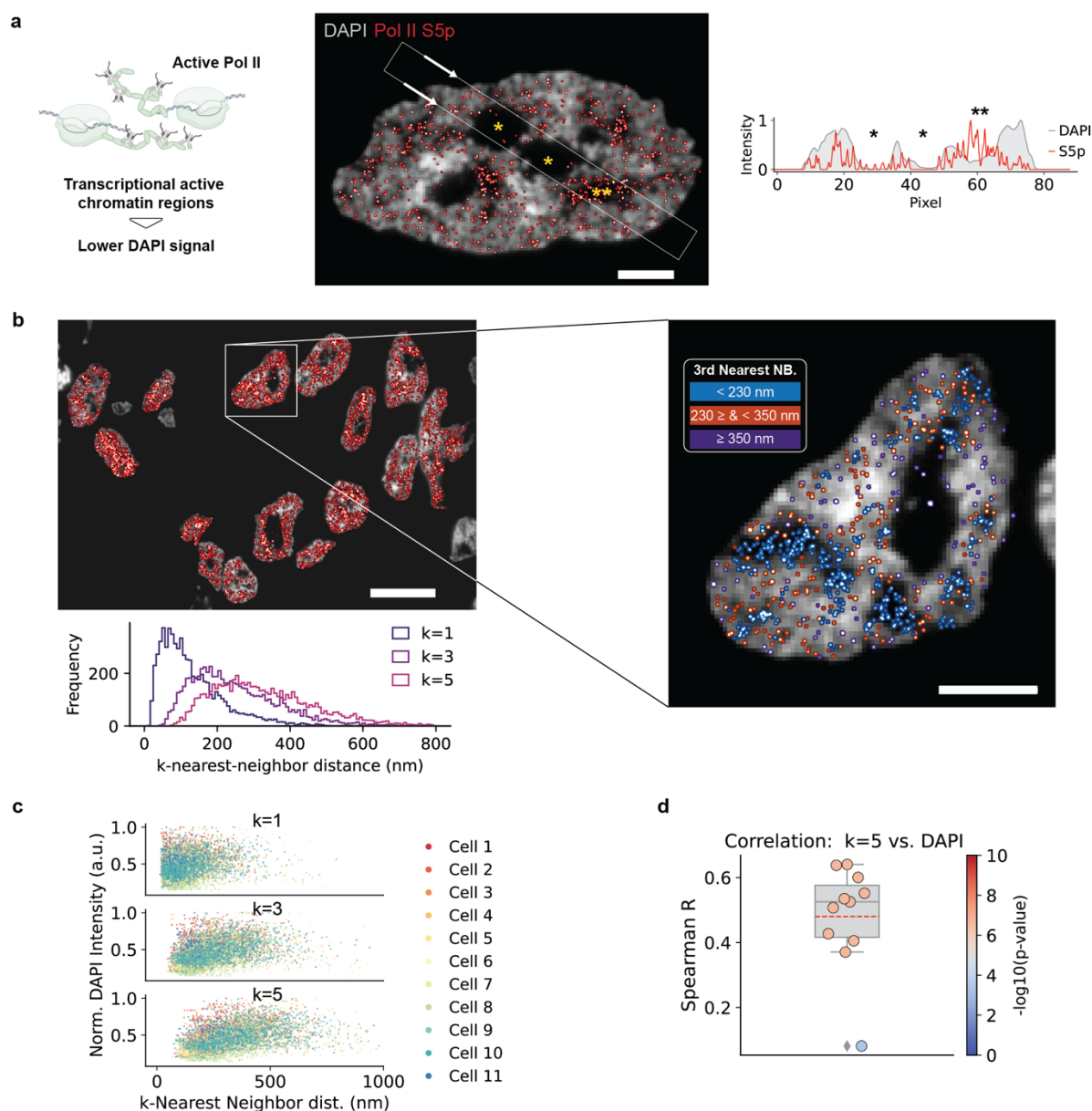
491
492 **Extended Data Fig. 4 | Pol II S5p correlation analysis DAPI vs. nearest neighbor distances. a**. Left: active Pol II associates with
493 euchromatin featuring lower DAPI intensities compared to A-T rich and densely-packed heterochromatin. Center: Pol II S5p
494 tkPAINT image including DAPI overlay (same as shown in **Fig. 2**a). Right: The line profiles below the image show the Pol II S5p and
495 DAPI signal distribution across the white box indicated in the center image. The box first crosses two DAPI-negative regions
496 without Pol II S5p signal (presumably nucleoli) followed by a third DAPI-negative region featuring high S5p signal. **b** Histogram of
497 k-nearest-neighbor distances (k=1,3,5) between Pol II S5p localization clouds for the data set shown in **Fig. 3**a. In the magnified
498 cell on the right localization clouds were colored according to their 3rd nearest neighbor distance (blue: <230 nm, red ≥ 230 nm
499 & < 350 nm; purple ≥ 350 nm). The rendering visually confirms that DAPI-weak regions feature higher local abundances of Pol II
500 S5p localization clouds[49,59]. Highly clustered Pol II (blue localization clouds) in DAPI weak areas likely correspond to nuclear

16

speckles. **c** To quantify the anti-correlation between DAPI intensity (as a degree of chromatin compactness) and Pol II S5p abundance, we plotted k-nearest neighbor distances vs. normalized DAPI intensity for all nuclei in the data set. Indeed, localization clouds with small k-nearest neighbor distances, indicating a high local abundance of the antigen, were associated with DAPI weaker regions. The correlation becomes more pronounced for higher order nearest neighbor distances. **d** We calculated the Spearman rank-order correlation coefficient (R) for each cell in the data set (n=11) for the 5th nearest neighbor distance of each localization cloud, confirming the correlation as highly significant (R≈0.5; p<0.0001). A correlation of <1 is expected since Pol II is absent from nucleoli, which are also DAPI weak nuclear regions. Scale bars, 10 μm in (b) and 3 μm in zoom in (b).
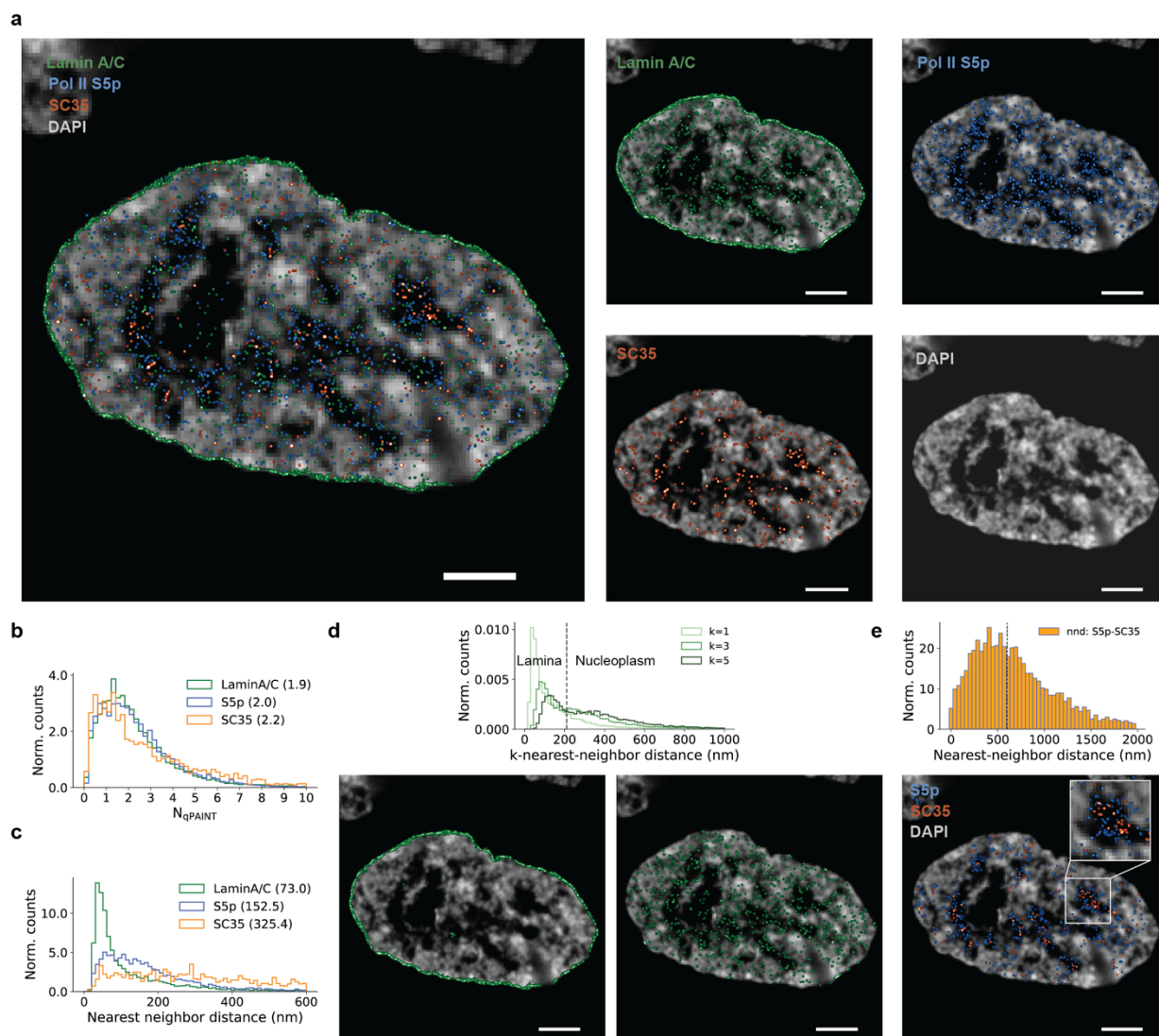
Extended Data Fig. 5 | Quantitative analysis of Exchange-tkPAINT: Lamin A/C, Pol II S5p, SC35. a Exchange-tkPAINT image of Lamin A/C, Pol II S5p and SC35 including DAPI image (same as in **Fig. 4**a), overlayed on the left and displayed individually on the right. **b** Histogram of qPAINT counting results obtained for Lamin A/C, Pol II S5p and SC35. **c** Histogram of nearest neighbor distances measured individually for Lamin A/C, Pol II S5p and SC35. **d** Top: inspection of higher order nearest neighbor distance histograms revealed two peaks, indicating the lamina-associated fraction and the nucleoplasmic fraction of Lamin A/C, as confirmed when filtering for each peak (black dashed line) and visualizing the spatial distribution in the images below. **e** Intermolecular nearest neighbor distance measurements between Pol II and SC35. Although both antigens are known to associate with nuclear speckles[59], the peak around 500 nm indicates a spatial segregation. Visualization of only Pol II S5p and SC35 localization clouds with a intermolecular distance <600 nm (black dashed line) in fact revealed a more centered organization of SC35 in DAPI-negative regions with S5p in the periphery, which has been similarly observed via genomics-based approaches[81]. Scale bars, 3 m in (a) and 1 m in zoom-in.

Online Methods

Materials. Unmodified, dye-labeled, and modified DNA oligonucleotides were purchased from Integrated DNA Technologies, Metabion and Biomers. Unmodified oligos were purified via standard desalting and modified oligos via HPLC. DNA scaffold strands were purchased from Tilibit (p7249, identical to M13mp18). Sample chambers were ordered from Ibidi GmbH (8-well 80827 and 18-well 81817). Tris 1M pH 8.0 (AM9856), EDTA 0.5M pH 8.0 (AM9261), Magnesium 1M (AM9530G) and Sodium Chloride 5M (AM9759) were ordered from Ambion. Streptavidin (S-888) Ultrapure water (15568025), PBS (20012050), 4',6-Diamidino-2-Phenylindole, Dihydrochloride (D1306) (A39255), BSA (AM2616) and TetraSpeck™ Microspheres 0.1 µm (T7279), DMEM (10569) and Dithiothreitol (DTT) were purchased from Thermo Fisher Scientific. BSA-Biotin (A8549), Tween-20 (P9416-50ML), Glycerol (cat. 65516-500ml), (+-)-6-Hydroxy-2,5,7,8-tetra-methylchromane-2-carboxylic acid (Trolox) (238813-5G), methanol (32213-2.5L), 3,4-dihydroxybenzoic acid (PCA) (37580-25G-F), protocatechuate 3,4-dioxygenase pseudomonas (PCD) (P8279-25UN), cell scrapers (CLS353085), Triton-X 100 (93443), Gelatin from cold fish skin (G7041-500G), Formamide (F9037), RNAse A (EN0531), Sodium Azide (S2002), HEPES (H4034-100G), FastAP Alkaline Phosphatase (EF0651), Methyl cellulose 25 CP (M6385-100G), Glycine (G8898), Sodium hydroxide (P3911-1kg), methyl cellulose (M6385), dextran sulfate (D4911) 20xSSC buffer (S6639)and sucrose (S0389) was purchased from Sigma-Aldrich. 10% fetal bovine serum was purchased from Genesee Scientific (25-514). EM grade paraformaldehyde (PFA) was purchased from Electron Microscopy Services (15714). 90 nm gold nanoparticles (G-90-20-10 OD10) were purchased from Cytodiagnostics. Primary anti-Lamin A/C (mouse, 34698), anti-LAMP1 (rabbit, 9091BF) and anti a-tubulin (rabbit, 2125BF) antibodies were purchased from Cell Signaling (mouse, 34698). Primary anti-Pol II CTD S5p (rabbit, ab5131), anti-Digoxigenin (mouse, ab420) and anti-SC35 (mouse, ab11826) antibodies were purchased from Abcam. Primary anti-Pol II CTD (mouse, CTD4H8) antibody was purchased from BioLegend. Secondary donkey anti-rabbit labeled with Alexa488 was purchased from Thermo Fisher Scientific (A21206). Secondary donkey anti-rabbit and (711-005-152) and goat anti-mouse (115-005-003) antibodies were purchased from Jackson ImmunoResearch Laboratories. DBCO-modified single domain antibodies against mouse IgG (N2005-DBCO) and rabbit IgG (N2405-DBCO) as well as mouse IgG multiplexing blocker(K0102-50) were purchased from NanoTag. 0.5-mL Amino Ultra Centrifugal Filters with 50 kDa and 10 kDa molecular weight cutoffs were purchased from Millipore (UFC5050 and UFC5010, respectively). DBCO-sulfo-NHS ester cross-linker was purchased from Vector Laboratories (CCT-A124). Qubit Protein Assay (Q33211), NuPage 4-12% Bis-Tris protein gels (NP0323BOX), NuPage LDS Sample Buffer (NP0007) was purchased from Invitrogen. InstantBlue Coomassie Protein Stain was purchased from Abcam (ab119211).

Buffers. Four buffers were used for sample preparation and imaging: Buffer A (10 mM Tris-HCl pH 7.5, 100 mM NaCl); Buffer B (5 mM Tris-HCl pH 8.0, 10 mM MgCl2, 1 mM EDTA); Buffer C (1× PBS, 500 mM NaCl); 10x folding buffer (100 mM Tris,10 mM EDTA pH 8.0, 125 mM MgCl2). Antibody storage buffer: 1% BSA, 0.1% Sodium Azide, 10 mM EDTA, 50% glycerol). Buffers were checked for pH. Imaging buffers were supplemented with oxygen scavenging & triplet state quenching system 1× PCA, 1× PCD, 1× Trolox prior to imaging.

PCA, PCD, Trolox. 100× Trolox: 100 mg Trolox, 430 µL 100% Methanol, 345 µL 1 M NaOH in 3.2 mL H2O. 40× PCA: 154 mg PCA was mixed with 10 mL water adjusted to pH 9.0 with NaOH. 100× PCD: 9.3 mg PCD, 13.3 mL of buffer (100 mM Tris-HCl pH 8, 50 mM KCl, 1 mM EDTA, 50% glycerol).

DNA origami design and assembly. DNA origami with 20-nm spaced docking strands ('20 nm grids') were designed previously using the Picasso Design[8] module. A list of all used DNA strands can be found in ref.[117].

570 Folding of structures was performed using the following components: single-stranded DNA scaffold
571 (0.01 µM), core staples (0.1 µM), biotin staples (0.01 µM), extended staples for DNA-PAINT (each 1 µM),
572 1x folding buffer in a total of 50 µl for each sample. Annealing was done by cooling the mixture from 80 °C
573 to 25 °C in 3 hours in a thermocycler. Using a 1:1 ratio between scaffold and biotin staples allows sample
574 preparation without prior DNA origami purification, where otherwise free biotinylated staples would
575 saturate the streptavidin surface and prevent origami immobilization on the glass surface. As docking
576 strand sequence, we used a 20nt adapter motif[16] (A20: AAGAAAGAAAAGAAGAAAAG), which allowed us
577 to later hybridize any desired docking strand imaging to the origami via a stably-binding complementary
578 adapter 'cA20_DS'. The adapter motif is cA20: CTTTTCTTCTTTTCTTTCTT which is concatenated to the
579 docking strand of choice DS (see **Supplementary Table 2** for sequences).

581 **DNA origami sample preparation**. Ibidi 8-well slides were prepared as follows. A 10 µl drop of biotin-
582 labeled bovine albumin (1 mg/ml, dissolved in buffer A) was placed at the chamber center and incubated
583 for 2 min and aspirated. The chamber was then washed with 200 µl of buffer A, aspirated, and then a 10
584 µl drop streptavidin (0.5 mg/ml, dissolved in buffer A) was placed at the chamber center and incubated
585 for 2 min. After aspirating and washing with 200 µl of buffer A and subsequently with 200 µl of buffer B,
586 a 10 µl of DNA origami (1:100-200 dilution in buffer B from folded stock) was placed at the chamber center
587 and incubated for 5 min. Next, the chamber was washed with 200 µl of Buffer B and docking strand
588 adapters hybridizing to the DNA origami were added at 100 nM in Buffer B, incubated for 5 min and
589 washed with 200 µl Buffer B. Finally, Buffer C and imager strand was added for DNA-PAINT imaging.

591 **Conjugation of secondary antibodies/nanobodies with docking strands**. DNA antibody conjugations
592 were performed in 0.5-mL Amino Ultra Centrifugal Filters with 50 kDa molecular weight cutoffs with
593 DBCO-sulfo-NHS ester cross-linker, which was dissolved at 20 mM DMSO and stored in single-use aliquots
594 at -80° C. This cross-linker links azide-functionalized DNA oligonucleotides to surface-exposed lysine
595 residues. Azide-functionalized DNA oligonucleotides were stored in 1 mM deionized water. Critically, all
596 antibodies were ordered carrier-free, as common preservatives such as bovine serum albumin and sodium
597 azide interfere with the conjugation reaction. First, 500 µL PBS was added to the Amicon filters, which
598 were centrifuged for 5 min at 10,000 rcf. After wetting the filters, 25 µg antibody was added and washed
599 twice with PBS. For each wash, PBS was added to a total volume of 500 µL, and the filters were centrifuged
600 for 5 min at 10,000 rcf. If after the second spin, the total volume remaining in each filter was greater than
601 100 µL, the filters were centrifuged again for 5 min at 10,000 rcf. After the second PBS wash, a 20-fold
602 molar excess of DBCO-sulfo-NHS ester cross-linker and a 20-fold molar excess of DNA oligonucleotide
603 were added, and after gentle mixing, each conjugation reaction was incubated in the dark at 4° C
604 overnight. The following day, conjugated antibodies were washed three times with PBS, as described
605 above. To elute the antibody, the filter was inverted in a fresh tube and centrifuged for 2 min at 1,500 rcf.
606 The conjugated antibody was transferred to a clean tube and stored at -20° C in antibody storage buffer.
607 Concentrations were measured using the Qubit Protein Assay. DNA-antibody conjugation was confirmed
608 by comparing unconjugated and conjugated antibodies on NuPage 4-12% Bis-Tris protein gels. For each
609 sample, 0.5 µg total protein was added to NuPage LDS Sample Buffer and 50 mM DTT. Protein was
610 denatured at 80° C for 10 min. Gels were run at 75 V for 5 min, then at 180 V for 60 min. Gels were stained
611 with InstantBlue Coomassie Protein Stain for 15 minutes at room temperature, rinsed with water, and
612 imaged on a Sapphire Biomolecular Imager (Azure Biosystems).
613 Conjugation of DBCO-modified nanobodies (also "single domain antibody") was performed analogously,
614 but in 0.5-mL Amino Ultra Centrifugal Filters with 50 kDa molecular weight cutoffs. After filter wetting and
615 washing, 25 µg nanobody was added and washed twice. For each wash, PBS was added to a total volume
616 of 500 µL, and the filters were centrifuged for 5 min at 10,000 rcf. After the second PBS wash, a 5-fold
617 molar excess of DNA oligonucleotide were added, and after gentle mixing, each conjugation reaction was

618 incubated in the dark at 4° C overnight. The next day, conjugated nanobodies were washed three times
619 and transferred to a clean tube for storage at -20° C in antibody storage buffer. Concentrations were
620 measured using the Qubit Protein Assay and working aliquots were adjusted to 5 mM in antibody storage
621 buffer as recommended by the manufacturer.
622
623 **Tissues**. Mouse tissue was obtained from naïve control mice meeting experimental endpoint on an
624 approved Harvard Medical School/Longwood Medical Area IACUC protocol.
625
626 **Cell culture and plating**. HeLa cells were maintained in DMEM supplemented with 10% fetal bovine serum
627 at 37 °C with 5% CO2 and were checked regularly for mycoplasma contamination. For imaging of whole
628 HeLa cells, ~16K cells were seeded in each well of an Ibidi 18-well chamber, placed in the incubator
629 overnight and fixed the following day. For preparation of cell pellets for cryosectioning, ~1 million cells
630 were seeded in 10-cm dishes and placed in the incubator until reaching 70 % confluency.
631
632 **HeLa cell preparation for cryosectioning.** HeLa cells were processed according to previously published
633 protocols[64]. In brief, HeLa cells were grown in 10 cm Petri dishes and once reaching 70 % confluence, were
634 fixed in 4% PFA 250 mM HEPES, pH 7.6 for 10 min. Fixative was decanted and cells further fixed with 8%
635 PFA in 250 mM HEPES, pH 7.6 for a total of 2h at 4°C. During fixation, cells were gently scraped off the
636 surface unidirectionally using cell scrapers previously soaked in fixative to avoid sticking. Detached cell
637 suspension was transferred into a 1.5 mL hydrophobic Eppendorf tube and centrifuged at increasing
638 speeds to form a pellet of fixed cells: 300 × g, 5 min; 500 × g, 2 min; 1,000 × g, 2 min; 2,000 × g, 2 min;
639 4,000 × g. At this point, the pellet could be resuspended in 1% PFA in 250 mM HEPES, pH 7.6 and stored
640 overnight at 4°C. Next, the pellet was transferred between several drops of 2.1 M sucrose drops to wash
641 away residual fixative and infiltrated 2-4h in 2.1 M sucrose (sucrose acts as cryoprotectant to prevent
642 structural damage during freezing. The pellet becomes transparent). Next, the infiltrated pellet was
643 transferred to a metal pin, residual sucrose carefully removed using filter paper and the pellet shaped into
644 a cone under a dissecting light microscope and using forceps. Finally, the cell pellet was frozen by
645 immersion into liquid nitrogen and was stored indefinitely in liquid nitrogen tanks. We would like to also
646 highlight alternative protocols based on gelatin embedding, which can improve probe handling as
647 discussed in a recent review[35].
648
649 **Tissue preparation for cryosectioning.** Mouse cerebellum and spleen were sectioned into 1-2 mm cubes
650 and incubated consecutively in 4% PFA 250 mM HEPES, pH 7.6, in 8% PFA in HEPES for 2 hours at 4°C, and
651 in 1% PFA in HEPES overnight at 4°C. Tissue cubes were then embedded in 7.5% gelatin, 10% Sucrose in
652 PBS (gelatin-sucrose solution was prepared at 70°C and stored in 10mL aliquots at -20°C). Tissues were
653 infiltrated in liquid gelatin-sucrose for 30 minutes at 37°C and subsequently solidified at 4°C. Then, the gel
654 block was removed from the tube, the tissue block cut out as 1mm blocks and transferred into 2.1 M
655 sucrose in PBS for 4h. Lastly, sucrose-infiltrated tissue blocks were placed on metal pins, residual sucrose
656 carefully removed using filter paper, frozen by immersion into liquid nitrogen and stored indefinitely in
657 liquid nitrogen tanks.
658
659 **Tokuyasu cryosectioning.** All Tokuyasu cryosectioning was performed at the Harvard Electron Microscopy
660 Core using a Leica EM UC7 Ultramicrotome equipped with a FC7 cryo-chamber. Frozen cell/tissue samples
661 were cut at a temperature of -110°C using a diamond knife (Diatome). Lastly, sections were collected using
662 drops a freshly prepared 1:1 mixture of 2.1 M sucrose in PBS and 2% methyl cellulose in water and
663 transferred onto Ibidi 8-well chambers for tkPAINT imaging, that had previously been glow discharged
664 (EMS100x, 2min at 40mA). Sectioned samples can be stored at -20°C for months.
665

666 **TEM imaging of Tokuyasu sections**. For transmission electron microscopy imaging, cryosections were
667 placed on formvar-coated grids, washed, and contrasted using methyl cellulose/uranyl acetate. TEM
668 imaging was performed at the Harvard Electron Microscopy Core on a JEOL 1200EX TEM.
669
670 **HeLa cell fixation, epon embedding and sectioning for TEM imaging**
671 HeLa cells were grown in 10 cm Petri dishes and once reaching 70 % confluence, were fixed in 4% PFA 250
672 mM HEPES, pH 7.6 for 15 min followed by three washes in PBS for 2 min each. For permeabilized samples,
673 permeabilization was applied in Petri dish, followed by three washes in PBS. Cells were gently scraped and
674 collected into a 0.5 mL tube and centrifuged at 200 × g for two min to form pellets. The solution was
675 exchanged and pellets stored in 1% PFA in 250 mM HEPES, pH 7.6 overnight at 4 °C. The next day, cell
676 pellets were postfixed with 1% Osmium Tetroxide (OsO4)/1.5% Potassium Ferrocyanide(KFeCN6) for 1
677 hour, washed 2× in water, 1× Maleate buffer (MB) 1× and incubated in 1 % uranyl acetate in MB for 1 hr
678 followed by 2 washes in water and subsequent dehydration in grades of alcohol (10 min each; 50%, 70%,
679 90%, 2×10min 100%). The samples were then put in propylene oxide for 1 h and infiltrated ON in a 1:1
680 mixture of propylene oxide and TAAB Epon (TAAB Laboratories Equipment Ltd, https://taab.co.uk). The
681 following day the samples were embedded in TAAB Epon and polymerized at 60 °C for 48 h. Ultrathin
682 sections (~80 nm) were cut on a Reichert Ultracut-S microtome, picked up onto copper grids, stained with
683 lead citrate and examined in a Tecnai Spirit BioTwin Transmission electron microscope. Images were
684 recorded with an AMT NanoSprint43-MkII camera.
685
686 **Immunogold TEM imaging**
687 Tokuyasu sectioning was performed at -120 °C and at ~80nm cryosection thickness. Sections were picked
688 up on a drop of 2.3 M sucrose with a small amount of 2% methyl cellulose added (9:1 mixture) and
689 transferred to formvar-carbon coated copper grids. Gold labeling was carried out at room temperature
690 on a piece of parafilm: antibodies were diluted in 1% BSA in PBS Grids, floated on drops of 1% BSA for 10
691 minutes to block for unspecific labeling, transferred to 5 µl drops of primary antibody and incubated for
692 30 minutes. Subsequently, grids were washed in 4 drops of PBS (total 10 min) before incubation in 10nm
693 Protein A-gold (University Medical Center, Utrecht, the Netherlands) for 20 min. Grids were washed in 2
694 drops of PBS followed by 4 drops of water (total 15 min). The labeled sections were contrasted and
695 embedded in methyl cellulose by floating the grids on a mixture of 0.3% uranyl acetate in 2% methyl
696 cellulose for 5 minutes before blotting excess liquid off on a filter paper. Grids were imaged on a JEOL
697 1200EX Transmission electron microscope and an AMT 2k CCD camera.
698
699 **Labeling of cryosections for tkPAINT**. 8-well chambers containing cryosections were thawed and washed
700 3× in PBS under agitation for 10min for sucrose removal and quenched with 100mM glycine in 100mM
701 HEPES for 15min. Next, cryosections were permeabilized in 0.3% Triton-X 100 in PBS for 5min, rinsed 3×
702 in PBS and ready for subsequent labeling. Note, that Tokuyasu immunogold protocols vary regarding
703 antibody incubation times. A general rule of thumb is using high antibody concentrations and short
704 incubation times, rather than low concentrations for extended incubations[17]. Hence, we chose relatively
705 high antibody dilutions (1:50-200) and could even observe strong antibody signal for incubations as short
706 as 5min. For a systematic investigation, antibody titration series can be advised. For our proof-of-concept
707 study we applied varying blocking and/or labeling conditions, which are listed in **Supplementary Table 1**
708 for all experiments with respect to blocking buffer as well as both antibody dilution and incubation times.
709 The blocking buffer was used for both antibody/nanobody incubations and as a washing solution in
710 between labeling in case of indirect primary and secondary antibody/nanobody labeling. After antibody
711 labeling, cryosections were washed 3× in PBS, stained with 30 nM DAPI in PBS for 3min and washed again
712 with PBS. For all tkPAINT experiments based on secondary nanobodies the samples were postfixed in 4%
713 PFA for 5 min, followed by three washes in PBS prior to imaging and DAPI staining. Lastly, Buffer C and

714   imager was added for tkPAINT imaging. Note that DAPI staining could faint for several rounds of washing,
715   especially for Exchange-PAINT experiments. However, staining could be simply recovered by performing
716   another round of DAPI staining at the same concentration as stated above.
717   *Phosphatase control (Fig. 2c)*. Two cryosection samples were processed as previously described until the
718   blocking step, at which they were placed for 1h at 37°C and one incubating with alkaline phosphatase to
719   remove phosphorylation site S5p as target antigen[59]. After washing 3× in PBS, normal blocking and indirect
720   immunostaining was performed using a fluorescently-labeled secondary antibody.
721   *Combined a-tubulin and telomere imaging (Fig. 4c)*. Cryosections were labeled for a-tubulin using primary
722   antibody + secondary antibody incubation and postfixed with 4% PFA in PBS for 10min followed by a
723   10min glycine quenching step. Next, the samples were washed with PBS, and incubated with 100-fold
724   diluted RNase A/T1 Mix in 1× PBS at 37 °C for 1 h. Samples were washed 3× in PBS, rinsed and incubated
725   with 50% formamide in 2× SSC for 15min. Next, the sample was placed on a heat block at 90 °C for 4.5 min
726   in 50% formamide in 2× SSC. A 20nt FISH probe against telomeric repeat (AACCCTAACCCTAACCCTAA
727   -A488) was added at 1 µm concentration in 20% formamide, 10% dextran sulfate and 4× SSC and
728   incubated overnight at 37°C for hybridization. Lastly, the sample was washed 2× with 20% formamide 2×
729   SSC, rinsed with PBS, and 30 nM DAPI in PBS for 3min was added. After a final wash in PBS, Buffer C was
730   added and imager for tkPAINT imaging. *mRNA imaging via poly(dT) probes (Fig. 4d)*. Cryosections were
731   treated as described until the blocking step, followed by a 10min wash in 4x SSC. Next, 40nt poly(dT) probe
732   modified with digoxigenin were added in 20% hybridization buffer (20% ethylene carbonate, 10% dextran
733   sulfate and 4× SSC) buffer at 37 °C overnight in a humidity chamber. The next day, the sample was washed
734   2× with 20% EC 2xSSCT for 15min, followed by three rinses with 4× SSC. The sample was then blocked
735   with 1% gelatin in PBS for 10min and subsequently subject to indirect immunostaining as described in
736   **Supplementary Table 1**. After final washes, Buffer C and imager was added for tkPAINT imaging.

737   **Fixation and labeling for whole HeLa cell imaging.** 24h after seeding HeLa cells in Ibidi 18-well chambers,
738   cells were fixed using 4% PFA 250 mM HEPES, pH 7.6 for 20min. Next, samples were washed 4× in PBS
739   (30s, 60s, 2×5 min) and both blocked and permeabilized in 3% BSA and 0.25% Triton X-100 in PBS at room
740   temperature for 90 min. Primary rabbit anti-Pol II S5p antibody was added at 1:100 in 3% BSA and 0.1%
741   Triton-X 100 in PBS and incubated overnight at 4 °C. The next morning, samples were washed 4x washes
742   in PBS (30s, 60s, 2× 5min) and DNA-conjugated secondary antibody (1:100) was added at 1:100 in 3% BSA
743   and 0.1% Triton-X 100 in PBCS and incubated for 1h at room temperature. Samples were quickly washed
744   3× in PBS, incubated with gold particles as fiducial markers (1:20 in PBS) for 5 min, washed again 2× in PBS
745   before adding Buffer C and imager for DNA-PAINT imaging.

746   **Super-resolution microscopy setup**. TIRF and HILO imaging was carried out at MicRoN Imaging Core at
747   Harvard Medical School on a Nikon Ti inverted microscope equipped with a Nikon Ti-TIRF-EM Motorized
748   Illuminator, a Nikon LUN-F Laser Launch with single fiber output (488nm, 90mW;561 nm, 70mW; 640nm,
749   65mW) and a Lumencore SpectraX LED Illumination unit. The objective-type TIRF system with an oil-
750   immersion objective (Apo TIRF 100×/1.49 DIC N2). DNA-PAINT experiments were performed using the 560
751   nm laser line and fluorescence emission was passed through a Chroma ZT 405/488/561/640 multi-band
752   pass dichroic mirror mounted on a Nikon TIRF filter cube located in the filter cube turret and a Chroma ET
753   595/50m band pass emission filter located on a Sutter emission filter wheel within the infinity space of
754   the stand before image recording on a line on a sCMOS camera (Andor, Zyla 4.2) mounted to a standard
755   Nikon camera port. For astigmatism-based 3D imaging, the C-mount side port of the microscope body was
756   replaced by a custom-built construction allowing to insert a cylindrical lens in front of the camera
757   (description including component list in **Supplementary Fig. 12**).
758

759 **Imaging conditions**. All fluorescence microscopy data was recorded with the sCMOS camera (2048 × 2048
760 pixels, pixel size: 6.5 µm). Both microscope and camera were operated with the Nikon Elements software
761 at 2×2 binning and cropped to the center 512 × 512 pixel field-of-view. The camera read out rate was set
762 to 200 MHz and the dynamic range to 16 bit. For detailed imaging parameters specific to the data
763 presented in all main and supplementary figures refer to **Supplementary Table 1**.

765 **Image analysis**. Please refer to **Supplementary Fig. 2** and **Supplementary Fig. 5** for a detailed step-by-
766 step illustration through all processing steps of super-resolution reconstruction. All DNA-PAINT/tkPAINT
767 imaging data was processed and reconstructed using the Picasso[8] software suite, Fiji[118,119] and previously-
768 published[16,116] and custom Python modules.

770 **Data availability**
771 All data are available in the main text or the supplementary materials, and materials are available upon
772 request.

774 **Code availability**
775 Super-resolution reconstruction was performed using the Picasso[8] suite developed by the Jungmann lab:
776 https://github.com/jungmannlab/picasso. Previously-published custom Python packages employed in
777 this study are available in public repositories: https://github.com/schwille-paint/picasso_addon and
778 https://github.com/schwille-paint/lbFCS2. Additional custom code will be made available upon request.

Author contributions

J.S. conceived the study, performed experiments, analyzed data and wrote the manuscript with input from all authors. M.E. performed cryosectioning, provided cryosection samples and performed TEM imaging. M.N. conjugated antibodies, maintained cell culture and provided cell samples for cryoblock preparations. L.M. prepared tissue cryoblocks and performed initial tissue tkPAINT experiments. S.A. contributed to initial joint experiments and to the manuscript storyline. R.B.M. performed antibody conjugations. L.B. developed code for chromatic aberration correction, nuclear volume calculation and contributed to the manuscript storyline. C.P.H. contributed to initial experiments. A.W. and L.A.-J. provided practical training and supported early protocol development J.W. provided helpful advice regarding cryosectioning and TEM data interpretation. P.Y. provided laboratory infrastructure, helpful advice and shared reagents. A.P. hosted a lab visit of J.S., provided training, protocols related to cryosectioning and valuable manuscript input. G.M.C. and C.-t.W. guided the project through joint discussions, valuable feedback and contributed to the manuscript storyline. All authors read and approved the final manuscript.

Competing interests

Potential conflicts of interest for G.M.C. are listed on https://arep.med.harvard.edu/t/. C.-t.W. holds or has patent filings pertaining to imaging, and her laboratory has held a sponsored research agreement with Bruker Inc. C.-t.W. is a co-founder of Acuity Spatial Genomics and, through personal connections to G.M.C, has equity in companies associated with him, including 10x Genomics and Twist. A.P. holds a patent on 'Genome Architecture Mapping'. P.Y. is also a co-founder, equity holder, director and consultant of Ultivue, Inc. and Digital Biology, Inc. All other authors declare no competing financial interest.

References

1. Vandereyken, K., Sifrim, A., Thienpont, B. & Voet, T. Methods and applications for single-cell and spatial multi-omics. *Nat Rev Genet* **24**, 494–515 (2023).
2. Dekker, J. *et al.* Spatial and temporal organization of the genome: Current state and future aims of the 4D nucleome project. *Molecular Cell* **83**, 2624–2640 (2023).
3. Rao, A., Barkley, D., França, G. S. & Yanai, I. Exploring tissue architecture using spatial transcriptomics. *Nature 2021 596:7871* **596**, 211–220 (2021).
4. Sahl, S. J., Hell, S. W. & Jakobs, S. Fluorescence nanoscopy in cell biology. *Nature Reviews Molecular Cell Biology 2017 18:11* **18**, 685–701 (2017).
5. Sauer, M. & Heilemann, M. Single-Molecule Localization Microscopy in Eukaryotes. *Chemical Reviews* **117**, 7478–7509 (2017).
6. Lelek, M. *et al.* Single-molecule localization microscopy. *Nature Reviews Methods Primers* **1**, 1–27 (2021).
7. Flores, V., Farabella, I. & Nir, G. Genome-wide tracing to decipher nuclear organization. *Current Opinion in Cell Biology* **82**, 102175 (2023).
8. Schnitzbauer, J., Strauss, M. T., Schlichthaerle, T., Schueder, F. & Jungmann, R. Super-resolution microscopy with DNA-PAINT. *Nature Protocols* **12**, 1198 (2017).
9. Jungmann, R. *et al.* Multiplexed 3D cellular super-resolution imaging with DNA-PAINT and Exchange-PAINT. *Nat Methods* **11**, 313–318 (2014).
10. Unterauer, E. M. *et al.* Spatial proteomics in neurons at single-protein resolution. *Cell* **187**, 1785-1800.e16 (2024).
11. Schueder, F. *et al.* Unraveling cellular complexity with transient adapters in highly multiplexed super-resolution imaging. *Cell* **187**, 1769-1784.e18 (2024).
12. Strauss, S. *et al.* Modified aptamers enable quantitative sub-10-nm cellular DNA-PAINT imaging. *Nature Methods* **15**, 685–688 (2018).
13. Fischer, L. S. *et al.* Quantitative single-protein imaging reveals molecular complex formation of integrin, talin, and kindlin during cell adhesion. *Nat Commun* **12**, 919 (2021).
14. Reinhardt, S. C. M. *et al.* Ångström-resolution fluorescence microscopy. *Nature* **617**, 711–716 (2023).
15. Jungmann, R. *et al.* Quantitative super-resolution imaging with qPAINT. *Nature Methods* **13**, 439 (2016).

16. Stein, J., Stehr, F., Jungmann, R. & Schwille, P. Calibration-free counting of low molecular copy numbers in single DNA-PAINT localization clusters. *Biophysical Reports* **1**, 100032 (2021).

17. Griffiths, G. *Fine Structure Immunocytochemistry*. (Springer Berlin Heidelberg, Berlin, Heidelberg, 1993). doi:10.1007/978-3-642-77095-1.

18. Schnell, U., Dijk, F., Sjollema, K. A. & Giepmans, B. N. G. Immunolabeling artifacts and the need for live-cell imaging. *Nat Methods* **9**, 152–158 (2012).

19. Humbel, B. M., de Jong, M. D. M., Müller, W. H. & Verkleij, A. J. Pre-embedding immunolabeling for electron microscopy: An evaluation of permeabilization methods and markers. *Microscopy Research and Technique* **42**, 43–58 (1998).

20. Irgen-Gioro, S., Yoshida, S., Walling, V. & Chong, S. Fixation can change the appearance of phase separation in living cells. *eLife* **11**, e79903 (2022).

21. Tanaka, K. A. K. *et al.* Membrane molecules mobile even after chemical fixation. *Nat Methods* **7**, 865–866 (2010).

22. Schueder, F. *et al.* Multiplexed 3D super-resolution imaging of whole cells using spinning disk confocal microscopy and DNA-PAINT. *Nature Communications* **8**, 2090 (2017).

23. Ghosh, A., Meub, M., Helmerich, D. A., Doose, S. & Sauer, M. Fast, whole-cell DNA-PAINT imaging with dual-labeled self-quenched imager probes. 2023.10.09.561472 Preprint at https://doi.org/10.1101/2023.10.09.561472 (2023).

24. Axelrod, D. Cell-substrate contacts illuminated by total internal reflection fluorescence. *The Journal of Cell Biology* **89**, 141 LP – 145 (1981).

25. Böger, C. *et al.* Super-resolution imaging and estimation of protein copy numbers at single synapses with DNA-point accumulation for imaging in nanoscale topography. *NPh* **6**, 035008 (2019).

26. Huang, K. *et al.* Quantitative, super-resolution localization of small RNAs with sRNA-PAINT. *Nucleic Acids Research* **48**, E96 (2020).

27. Marcano-García, L. F. *et al.* Quantitative Analysis of Protein–Protein Equilibrium Constants in Cellular Environments Using Single-Molecule Localization Microscopy. *Nano Lett.* (2024) doi:10.1021/acs.nanolett.4c04394.

28. Jayasinghe, I. *et al.* True Molecular Scale Visualization of Variable Clustering Properties of Ryanodine Receptors. *Cell Reports* **22**, 557–567 (2018).

29. Geiger, B., Tokuyasu, K. T. & Singer, S. J. Immunocytochemical localization of alpha-actinin in intestinal epithelial cells. *Proceedings of the National Academy of Sciences* **76**, 2833–2837 (1979).

30. Pombo, A., Hollinshead, M. & Cook, P. R. Bridging the resolution gap: Imaging the same transcription factories in cryosections by light and electron microscopy. *Journal of Histochemistry and Cytochemistry* **47**, 471–480 (1999).

31. Schwarz, H. & Humbel, B. M. Correlative Light and Electron Microscopy Using Immunolabeled Resin Sections. in *Electron Microscopy: Methods and Protocols* (ed. Kuo, J.) 229–256 (Humana Press, Totowa, NJ, 2007). doi:10.1007/978-1-59745-294-6_12.

32. Vicidomini, G. *et al.* High Data Output and Automated 3D Correlative Light–Electron Microscopy Method. *Traffic* **9**, 1828–1838 (2008).

33. Betzig, E. *et al.* Imaging Intracellular Fluorescent Proteins at Nanometer Resolution. *Science* **313**, 1642–1645 (2006).

34. Kopek, B. G. *et al.* Diverse protocols for correlative super-resolution fluorescence imaging and electron microscopy of chemically fixed samples. *Nat Protoc* **12**, 916–946 (2017).

35. Möbius, W. & Posthuma, G. Sugar and ice: Immunoelectron microscopy using cryosections according to the Tokuyasu method. *Tissue and Cell* **57**, 90–102 (2019).

36. Nanguneri, S., Flottmann, B., Horstmann, H., Heilemann, M. & Kuner, T. Three-Dimensional, Tomographic Super-Resolution Fluorescence Imaging of Serially Sectioned Thick Samples. *PLOS ONE* **7**, e38098 (2012).

37. Kopek, B. G., Shtengel, G., Xu, C. S., Clayton, D. A. & Hess, H. F. Correlative 3D superresolution fluorescence and electron microscopy reveal the relationship of mitochondrial nucleoids to membranes. *Proceedings of the National Academy of Sciences* **109**, 6136–6141 (2012).

38. Perkovic, M. *et al.* Correlative Light- and Electron Microscopy with chemical tags. *Journal of Structural Biology* **186**, 205–213 (2014).

39. Sigal, Y. M., Speer, C. M., Babcock, H. P. & Zhuang, X. Mapping Synaptic Input Fields of Neurons with Super-Resolution Imaging. *Cell* **163**, 493–505 (2015).

40. Franke, C. *et al.* Correlative single-molecule localization microscopy and electron tomography reveals endosome nanoscale domains. *Traffic* **20**, 601–617 (2019).

41. Wang, Y. *et al.* Rapid Sequential in Situ Multiplexing with DNA Exchange Imaging in Neuronal Cells and Tissues. *Nano Letters* **17**, 6131–6139 (2017).

42. Park, S. *et al.* Superresolution fluorescence microscopy for 3D reconstruction of thick samples. *Mol Brain* **11**, 17 (2018).

43. Clowsley, A. H. *et al.* Repeat DNA-PAINT suppresses background and non-specific signals in optical nanoscopy. *Nature Communications* **12**, 1–10 (2021).

44. Rames, M. J. *et al.* Multiplexed and Millimeter-Scale Fluorescence Nanoscopy of Cells and Tissue Sections via Prism-Illumination and Microfluidics-Enhanced DNA-PAINT. *Chemical & Biomedical Imaging* (2023) doi:10.1021/cbmi.3c00060.

909 45. Colom-Cadena, M. *et al.* Synaptic oligomeric tau in Alzheimer's disease — A potential culprit in the spread of tau pathology
910   through the brain. *Neuron* **111**, 2170-2183.e6 (2023).
911 46. Tokuyasu, K. T. A TECHNIQUE FOR ULTRACRYOTOMY OF CELL SUSPENSIONS AND TISSUES. *Journal of Cell Biology* **57**, 551–
912   565 (1973).
913 47. Narayanasamy, K. K. *et al.* Visualizing Synaptic Multi-Protein Patterns of Neuronal Tissue With DNA-Assisted Single-
914   Molecule Localization Microscopy. *Frontiers in Synaptic Neuroscience* **13**, (2021).
915 48. Narayanasamy, K. K., Rahm, J. V., Tourani, S. & Heilemann, M. Fast DNA-PAINT imaging using a deep neural network. *Nat Commun* **13**, 5047 (2022).
916   *Commun* **13**, 5047 (2022).
917 49. Guillot, P. V., Xie, S. Q., Hollinshead, M. & Pombo, A. Fixation-induced redistribution of hyperphosphorylated RNA
918   polymerase II in the nucleus of human cells. *Experimental Cell Research* **295**, 460–468 (2004).
919 50. Beliveau, B. J. *et al.* In situ super-resolution imaging of genomic DNA with oligoSTORM and oligoDNA-PAINT. in *Methods in
920   Molecular Biology* vol. 1663 231–252 (Humana Press Inc., 2017).
921 51. Otterstrom, J. *et al.* Super-resolution microscopy reveals how histone tail acetylation affects DNA compaction within
922   nucleosomes in vivo. *Nucleic acids research* **47**, 8470–8484 (2019).
923 52. Castells-Garcia, A. *et al.* Super resolution microscopy reveals how elongating RNA polymerase II and nascent RNA interact
924   with nucleosome clutches. *Nucleic Acids Research* **50**, 175–190 (2022).
925 53. Frottin, F. *et al.* The nucleolus functions as a phase-separated protein quality control compartment. *Science* **365**, 342–347
926   (2019).
927 54. Sasaki, H. M., Kishi, J. Y., Wu, C., Beliveau, B. J. & Yin, P. Quantitative multiplexed imaging of chromatin ultrastructure with
928   Decode-PAINT. *bioRxiv* 2022.08.01.502089 (2022) doi:10.1101/2022.08.01.502089.
929 55. Lein, E., Borm, L. E. & Linnarsson, S. The promise of spatial transcriptomics for neuroscience in the era of molecular cell
930   typing. *Science* **358**, 64–69 (2017).
931 56. Longo, S. K., Guo, M. G., Ji, A. L. & Khavari, P. A. Integrating single-cell and spatial transcriptomics to elucidate intercellular
932   tissue dynamics. *Nature Reviews Genetics 2021 22:10* **22**, 627–644 (2021).
933 57. Micheva, K. D. & Smith, S. J. Array Tomography: A New Tool for Imaging the Molecular Architecture and Ultrastructure of
934   Neural Circuits. *Neuron* **55**, 25–36 (2007).
935 58. Kimura, H. & Sato, Y. Imaging transcription elongation dynamics by new technologies unveils the organization of initiation
936   and elongation in transcription factories. *Current Opinion in Cell Biology* **74**, 71–79 (2022).
937 59. Xie, S. Q., Martin, S., Guillot, P. V., Bentley, D. L. & Pombo, A. Splicing Speckles Are Not Reservoirs of RNA Polymerase II,
938   but Contain an Inactive Form, Phosphorylated on Serine2 Residues of the C-Terminal Domain. *Molecular Biology of the Cell*
939   **17**, (2006).
940 60. Strauss, S. & Jungmann, R. Up to 100-fold speed-up and multiplexing in optimized DNA-PAINT. *Nature Methods* **17**, 1–3
941   (2020).
942 61. Niederauer, C. *et al.* Direct characterization of the evanescent field in objective-type total internal reflection fluorescence
943   microscopy. *Optics Express* **26**, 20492–20506 (2018).
944 62. Endesfelder, U., Malkusch, S., Fricke, F. & Heilemann, M. A simple method to estimate the average localization precision of
945   a single-molecule localization microscopy experiment. *Histochemistry and Cell Biology* **141**, 629–638 (2014).
946 63. H Chung, K. K. *et al.* Fluorogenic DNA-PAINT for faster, low-background super-resolution imaging. *Nature Methods* (2022)
947   doi:10.1038/s41592-022-01464-9.
948 64. Rothemund, P. W. K. Folding DNA to create nanoscale shapes and patterns. *Nature* **440**, 297 (2006).
949 65. Bond, C., Hugelier, S., Xing, J., Sorokina, E. M. & Lakadamyali, M. Heterogeneity of late endosome/lysosomes shown by
950   multiplexed DNA-PAINT imaging. *Journal of Cell Biology* **224**, e202403116 (2024).
951 66. Branco, M. R., Xie, S. Q., Martin, S. & Pombo, A. Correlative microscopy using Tokuyasu cryosections: applications for
952   immunogold labelling and in situ hybridisation. in *Cell Imaging (Methods Express Series)* (ed. Stephens, D.) 201–217 (Scion
953   Publishing, Bloxham, 2006).
954 67. Wade, O. K. *et al.* 124-Color Super-resolution Imaging by Engineering DNA-PAINT Blinking Kinetics. *Nano Letters* **19**, 2641–
955   2646 (2019).
956 68. Stein, J. *et al.* Toward Absolute Molecular Numbers in DNA-PAINT. *Nano Letters* **19**, 8182–8190 (2019).
957 69. Ester, M., Kriegel, H.-P., Sander, J. & Xu, X. A Density-Based Algorithm for Discovering Clusters in Large Spatial Databases
958   with Noise. *Proceedings of the 2nd International Conference on Knowledge Discovery and Data Mining* 226–231 (1996).
959 70. Schueder, F. *et al.* An order of magnitude faster DNA-PAINT imaging by optimized sequence design and buffer conditions.
960   *Nature Methods* **16**, 1101–1104 (2019).
961 71. Liu, S., Hoess, P. & Ries, J. Super-Resolution Microscopy for Structural Cell Biology. *Annual Review of Biophysics* **51**, 301–
962   326 (2022).
963 72. Pombo, A. *et al.* Regional specialization in human nuclei: visualization of discrete sites of transcription by RNA polymerase
964   III. *The EMBO Journal* **18**, 2241–2253 (1999).

26

73. Kimura, H., Tao, Y., Roeder, R. G. & Cook, P. R. Quantitation of RNA Polymerase II and Its Transcription Factors in an HeLa Cell: Little Soluble Holoenzyme but Significant Amounts of Polymerases Attached to the Nuclear Substructure. *Molecular and Cellular Biology* **19**, 5383–5392 (1999).

74. Boehning, M. *et al.* RNA polymerase II clustering through carboxy-terminal domain phase separation. *Nat Struct Mol Biol* **25**, 833–840 (2018).

75. Kim, J., Venkata, N. C., Hernandez Gonzalez, G. A., Khanna, N. & Belmont, A. S. Gene expression amplification by nuclear speckle association. *Journal of Cell Biology* **219**, e201904046 (2019).

76. Xie, S. Q., Lavitas, L. M. & Pombo, A. CryoFISH: fluorescence in situ hybridization on ultrathin cryosections. *Methods in molecular biology (Clifton, N.J.)* **659**, 219–230 (2010).

77. Agasti, S. S. *et al.* DNA-barcoded labeling probes for highly multiplexed Exchange-PAINT imaging. *Chemical Science* **8**, 3080–3091 (2017).

78. Ilik, İ. A. *et al.* SON and SRRM2 are essential for nuclear speckle formation. *eLife* **9**, e60579 (2020).

79. Dechat, T. *et al.* Nuclear lamins: major factors in the structural organization and function of the nucleus and chromatin. *Genes Dev.* **22**, 832–853 (2008).

80. Ikegami, K., Secchia, S., Almakki, O., Lieb, J. D. & Moskowitz, I. P. Phosphorylated Lamin A/C in the Nuclear Interior Binds Active Enhancers Associated with Abnormal Transcription in Progeria. *Developmental Cell* **52**, 699-713.e11 (2020).

81. Chen, Y. *et al.* Mapping 3D genome organization relative to nuclear compartments using TSA-Seq as a cytological ruler. *Journal of Cell Biology* **217**, 4025–4048 (2018).

82. Branco, M. R. & Pombo, A. Intermingling of Chromosome Territories in Interphase Suggests Role in Translocations and Transcription-Dependent Associations. *PLOS Biology* **4**, e138 (2006).

83. Ferrai, C. *et al.* Poised Transcription Factories Prime Silent uPA Gene Prior to Activation. *PLOS Biology* **8**, e1000270 (2010).

84. Huang, B., Wang, W., Bates, M. & Zhuang, X. Three-Dimensional Super-Resolution Imaging by Stochastic Optical Reconstruction Microscopy. *Science* **319**, 810813 (2008).

85. Franke, C. *et al.* Approach to map nanotopography of cell surface receptors. *Commun Biol* **5**, 1–16 (2022).

86. Stierhof, Y.-D., Schwarz, H. & Frank, H. Transverse sectioning of plastic-embedded immunolabeled cryosections: Morphology and permeability to protein A-colloidal gold complexes. *Journal of Ultrastructure and Molecular Structure Research* **97**, 187–196 (1986).

87. Beliveau, B. J. *et al.* Versatile design and synthesis platform for visualizing genomes with Oligopaint FISH probes. *Proceedings of the National Academy of Sciences of the United States of America* **109**, 21301–21306 (2012).

88. Chen, K. H., Boettiger, A. N., Moffitt, J. R., Wang, S. & Zhuang, X. Spatially resolved, highly multiplexed RNA profiling in single cells. *Science* **348**, aaa6090–aaa6090 (2015).

89. Eng, C. H. L. *et al.* Transcriptome-scale super-resolved imaging in tissues by RNA seqFISH+. *Nature* **568**, 235–239 (2019).

90. Lee, J. H. *et al.* Highly multiplexed subcellular RNA sequencing in situ. *Science* **343**, 1360–1363 (2014).

91. Nguyen, H. Q. *et al.* 3D mapping and accelerated super-resolution imaging of the human genome using in situ sequencing. *Nature Methods* **17**, 822–832 (2020).

92. Kohman, R. E. & Church, G. M. Fluorescent in situ sequencing of DNA barcoded antibodies. *bioRxiv* 2020.04.27.060624 (2020) doi:10.1101/2020.04.27.060624.

93. Li, Y. *et al.* Real-time 3D single-molecule localization using experimental point spread functions. *Nature Methods* **15**, 367 (2018).

94. Fu, S. *et al.* Field-dependent deep learning enables high-throughput whole-cell 3D super-resolution imaging. *Nat Methods* **20**, 459–468 (2023).

95. Thiele, J. C. *et al.* Isotropic three-dimensional dual-color super-resolution microscopy with metal-induced energy transfer. *Science Advances* **8**, eabo2506 (2022).

96. Huang, F. *et al.* Ultra-High Resolution 3D Imaging of Whole Cells. *Cell* **166**, 1028–1040 (2016).

97. Shtengel, G. *et al.* Interferometric fluorescent super-resolution microscopy resolves 3D cellular ultrastructure. *Proceedings of the National Academy of Sciences* **106**, 3125–3130 (2009).

98. Bates, M. *et al.* Optimal precision and accuracy in 4Pi-STORM using dynamic spline PSF models. *Nat Methods* **19**, 603–612 (2022).

99. Balzarotti, F. *et al.* Nanometer resolution imaging and tracking of fluorescent molecules with minimal photon fluxes. *Science* **355**, 606–612 (2017).

100. van Elsland, D. M. *et al.* Ultrastructural Imaging of Salmonella–Host Interactions Using Super-resolution Correlative Light-Electron Microscopy of Bioorthogonal Pathogens. *ChemBioChem* **19**, 1766–1770 (2018).

101. van der Beek, J., de Heus, C., Liv, N. & Klumperman, J. Quantitative correlative microscopy reveals the ultrastructural distribution of endogenous endosomal proteins. *Journal of Cell Biology* **221**, e202106044 (2021).

102. Sograte-Idrissi, S. *et al.* Nanobody Detection of Standard Fluorescent Proteins Enables Multi-Target DNA-PAINT with High Resolution and Minimal Displacement Errors. *Cells* **8**, 48 (2019).

103. Götzke, H. *et al.* The ALFA-tag is a highly versatile tool for nanobody-based bioscience applications. *Nat Commun* **10**, 4403 (2019).

1023 104. Kuhlemann, A. *et al.* Genetic Code Expansion and Click-Chemistry Labeling to Visualize GABA-A Receptors by Super-
1024 Resolution Microscopy. *Front. Synaptic Neurosci.* **13**, (2021).
1025 105. van Donselaar, E., Posthuma, G., Zeuschner, D., Humbel, B. M. & Slot, J. W. Immunogold Labeling of Cryosections from
1026 High-Pressure Frozen Cells. *Traffic* **8**, 471–485 (2007).
1027 106. D'Este, E., Lukinavičius, G., Lincoln, R., Opazo, F. & Fornasiero, E. F. Advancing cell biology with nanoscale fluorescence
1028 imaging: essential practical considerations. *Trends in Cell Biology* **0**, (2024).
1029 107. Webster, P. & Webster, A. Cryosectioning Fixed and Cryoprotected Biological Material for Immunocytochemistry. in
1030 *Electron Microscopy: Methods and Protocols* (ed. Kuo, J.) 273–313 (Humana Press, Totowa, NJ, 2014). doi:10.1007/978-1-
1031 62703-776-1_13.
1032 108. Nehme, E., Weiss, L. E., Michaeli, T. & Shechtman, Y. Deep-STORM: super-resolution single-molecule microscopy by deep
1033 learning. *Optica, OPTICA* **5**, 458–464 (2018).
1034 109. Ouyang, W., Aristov, A., Lelek, M., Hao, X. & Zimmer, C. Deep learning massively accelerates super-resolution localization
1035 microscopy. *Nat Biotechnol* **36**, 460–468 (2018).
1036 110. Ricci, M. A., Manzo, C., García-Parajo, M. F., Lakadamyali, M. & Cosma, M. P. Chromatin Fibers Are Formed by
1037 Heterogeneous Groups of Nucleosomes In Vivo. *Cell* **160**, 1145–1158 (2015).
1038 111. Marenda, M., Lazarova, E., van de Linde, S., Gilbert, N. & Michieletto, D. Parameter-free molecular super-structures
1039 quantification in single-molecule localization microscopy. *Journal of Cell Biology* **220**, e202010003 (2021).
1040 112. Gómez-García, P. A. *et al.* Mesoscale Modeling and Single-Nucleosome Tracking Reveal Remodeling of Clutch Folding and
1041 Dynamics in Stem Cell Differentiation. *Cell Reports* **34**, 108614 (2021).
1042 113. Hansen, A. S., Pustova, I., Cattoglio, C., Tjian, R. & Darzacq, X. CTCF and cohesin regulate chromatin loop stability with
1043 distinct dynamics. *eLife* **6**, e25776 (2017).
1044 114. Gu, B. *et al.* Opposing Effects of Cohesin and Transcription on CTCF Organization Revealed by Super-resolution Imaging.
1045 *Molecular Cell* **80**, 699-711.e7 (2020).
1046 115. Gelléri, M. *et al.* True-to-scale DNA-density maps correlate with major accessibility differences between active and inactive
1047 chromatin. *Cell Reports* **42**, 112567 (2023).
1048 116. Stehr, F. *et al.* Tracking single particles for hours via continuous DNA-mediated fluorophore exchange. *Nature
1049 Communications 2021 12:1* **12**, 1–8 (2021).
1050 117. Stehr, F., Stein, J., Schueder, F., Schwille, P. & Jungmann, R. Flat-top TIRF illumination boosts DNA-PAINT imaging and
1051 quantification. *Nature Communications* **10**, 1268 (2019).
1052 118. Schindelin, J. *et al.* Fiji: an open-source platform for biological-image analysis. *Nat Methods* **9**, 676–682 (2012).
1053 119. Preibisch, S., Saalfeld, S., Schindelin, J. & Tomancak, P. Software for bead-based registration of selective plane illumination
1054 microscopy data. *Nat Methods* **7**, 418–419 (2010).
1055
1056
1057

28